Abelian origin of $\nu = 2/3$ and $2 + 2/3$ fractional quantum Hall effect

Liangdong Hu [1,2,3,4] and W. Zhu[2,3,4]

[1]*Zhejiang University, Hangzhou 310027, China*
[2]*School of Science, Westlake University, 18 Shilongshan Road, Hangzhou 310024, Zhejiang Province, China*
[3]*Institute of Natural Sciences, Westlake Institute for Advanced Study, 18 Shilongshan Road, Hangzhou 310024, Zhejiang Province, China*
[4]*Key Laboratory for Quantum Materials of Zhejiang Province, School of Science, Westlake University,*
18 Shilongshan Road, Hangzhou 310024, Zhejiang Province, China

We investigate the ground-state properties of the fractional quantum Hall effect at the filling factor $\nu = 2/3$ and $2 + 2/3$, with a special focus on their typical edge physics. Via a topological characterization scheme in the framework of the density matrix renormalization group, the nature of the $\nu = 2/3$ and $2 + 2/3$ states is identified as an Abelian hole-type Laughlin state, as evidenced by the fingerprint of entanglement spectra, central charge, and topological spin. Crucially, by constructing an interface between the $2/3$ ($2 + 2/3$) state and different integer quantum Hall states, we study the structures of the interfaces from many aspects, including charge density and dipole moment. In particular, we demonstrate the edge reconstruction by visualizing edge channels comprised of two groups: the outermost $1/3$ channel and the inner composite channel made of a charged mode and neutral modes.

I. INTRODUCTION

The fractional quantum Hall (FQH) [1,2] effect is a typical example of a topologically ordered state [3], and it has attracted a lot of attention since its discovery. The FQH state exhibits novel features of topological order, including fractional charge excitation [2], anyonic statistics, and the topologically protected edge property [4]. In particular, the study of edge physics is in the central stage of the FQH effect. First, due to the well-established bulk-edge correspondence, the knowledge of edge physics, which is more accessible in transport experiments, could provide insight into the topology in the bulk. In this context, the robustness of transport properties such as the quantization of electrical and thermal conductance can be intuitively understood by the formation of edge states. Second, beyond the description of topological order in the bulk, the interplay between strong interactions and confining potentials may "reshape" the FQH edge states, leading to the phenomenon of edge reconstruction [5–8], which introduces complications into edge physics. This has also motivated recent experimental efforts to detect the emergent neutral modes [9–13]. To sum up, edge physics, in the presence of tunneling and disorder, is an enduring theme in the study of the FQH effect.

In this paper, we will consider the FQH state at a filling factor of $\nu = 2/3$ in the lowest Landau level. The spin-polarized $\nu = 2/3$ FQH state is usually regarded as a particle-hole-conjugated Laughlin $\nu = 1/3$ state or, equivalently, a hole $1/3$ state embedded in the integer quantum Hall $\nu = 1$ background [14]. This is the simplest example with counterpropagating edge modes, thus the nature of the $2/3$ state has been widely studied both theoretically and experimentally [14–35]. In

particular, the upstream neutral edge mode has recently been identified in experiments [9–13], together with a more delicate indication of edge reconstruction [36–39]. One of our motivations is to provide clear evidence of possible edge reconstruction of the $2/3$ state and to uncover its connection with the experimental observations [9,10].

Additionally, we will also consider the FQH state at the filling factor $\nu = 2/3$ in the second Landau level (referred to as the $2 + 2/3$ or $8/3$ state). Apart from the bulk property of the $2 + 2/3$ state, edge physics and the associated edge reconstruction have never been discussed before. Moreover, due to the possibility of non-Abelian states in the second Landau level, the $2 + 2/3$ state may potentially realize non-Abelian-type topological order, such as the Z_4 parafermion FQH state [40,41], the Fibonacci $\hat{su}(3)_2$ state [42], and the Bonderson-Slingerland state [43]. To the best of our knowledge, the precise nature of edge physics of the $2 + 2/3$ state and the trace of non-Abelian predictions have not been studied systematically before [18,19], which is another motivation of this work.

In this paper, we present a microscopic study of the $\nu = 2/3$ and $2 + 2/3$ states based on the cylinder geometry from the viewpoints of bulk and edge properties. First of all, through a topological characterization scheme for bulk properties, we identify that both $2/3$ and $2 + 2/3$ states are topologically equivalent to a hole-type Laughlin state with Abelian statistics, based on the numerical evidence from the entanglement spectra and momentum polarization. Apart from the topological characters in the bulk, we are able to study the topological order by investigating the interface between $2/3$ ($2 + 2/3$) and different integer quantum Hall (IQH) states, and these manmade interfaces provide a method to

study a variety of edge as well as interface physics. In particular, we find strong signals for edge reconstruction on the $\nu = 0|\nu = 2/3$ and $\nu = 2|\nu = 2 + 2/3$ interfaces, and we identify that the outer and inner edges are located at density changes of $0 \rightarrow 1/3$ and $1/3 \rightarrow 2/3$, respectively. These results not only test predictions of the effective-field theory, but they also provide further insight into the physics of edge reconstruction.

Moreover, we contribute two different methods to obtain the topological shift quantum number [44], which provides ambiguous information for the $\nu = 2/3, 2 + 2/3$ states. One method is through momentum polarization from entanglement spectra [45,46], which is based on a uniform bulk state. The other method is via electric dipole momenta living on the FQH edge or interface [47]. In particular, both of these methods give the same topological shift, where $\mathcal{S} = 0$ for the $\nu = 2/3$ state and $\mathcal{S} = 2$ for the $\nu = 8/3$ state. In Appendix B, the theoretical topological shift of a fully polarized Abelian $\nu = 2/3$ state in a higher Landau level [i.e., $\nu = n + 2/3$ ($n = 0, 1, 2, \dots$)] is $\mathcal{S} = 2n$. This provides additional evidence of the Abelian nature of these two states.

The rest of the paper is organized as follows. In Sec. II we will illustrate the details of implementing DMRG in a FQH system and the construction of an interface in DMRG. We will summarize the quantum numbers that determine the topological order in the bulk, on the edge of FQH states. As a result, in Sec. III we will show the topological characters of $\nu = 1/3, 2/3, 8/3$ states. Finally, in Secs. IV and V we will study the edge and interface physics between FQH ($\nu = 1/3, 2/3, 8/3$) and IQH states ($\nu = 0, 1, 2, 3$).

II. MODEL AND METHOD

A. Model

Throughout this paper, we consider interacting electrons living on the cylinder geometry in the presence of a uniform perpendicular magnetic field. The cylinder has area $S = L_x L_y$, where y runs along the periodic direction with circumference $L_y = L$, and x runs along the open direction with length L_x. In the Landau gauge $\mathbf{A} = (0, -Bx)$ and magnetic field $\mathbf{B} = -\mathbf{e}_z B$ (or $B_z = -B$, where $\mathbf{e}$ is the unit vector), the single-particle orbit in the nth-Landau level (nth-LL) is

$$\psi_{n,j}(\mathbf{r}) = \frac{e^{i\frac{X_j}{\ell^2}y - \frac{(x-X_j)^2}{2\ell^2}}}{\sqrt{2^n n! \sqrt{\pi} \ell L_y}} H_n\left(\frac{x-X_j}{\ell}\right), \quad (1)$$

where $H_n(x)$ is the nth-order Hermite polynomial, $\ell = \sqrt{\hbar/|eB|}$ is the magnetic length, and $X_j = k_j \ell^2$ is the center of a single-particle orbit. There are N_ϕ-fold-degenerate orbitals in a single Landau level $2\pi \ell^2 N_\phi = L_x L_y$, which are distinguished by the momentum quantum number $k_j = \frac{2\pi j}{L_y}$ ($j = 0, 1, \dots, N_\phi - 1$). When a single LL is partially occupied with a fractional filling factor $\nu = N_e/N_\phi = p/q$ (p and q are integers and coprime to each other), one can consider the electron-electron interaction by projecting onto the Nth Landau level (LL):

$$\hat{H}_I = \sum_{j_1, j_2, j_3, j_4}^{N_\phi} A_{j_1, j_2, j_3, j_4}^N \hat{c}_{j_1}^\dagger \hat{c}_{j_2}^\dagger \hat{c}_{j_3} \hat{c}_{j_4}. \quad (2)$$

In this paper, we adopt two types of interactions, namely the Haldane pseudopotential and the modified Coulomb interaction $V(r) = \frac{e^2}{\epsilon r} e^{-r^2/\xi^2}$ with a regulated length $\xi = 4\ell$ [48]. More details about the derivation of A_{j_1, j_2, j_3, j_4}^N can be found in Appendix A. We only show the result here,

$$A_{j_1, j_2, j_3, j_4}^N = \frac{1}{2L_y} \int_{-\infty}^{\infty} dq_x \sum_{q_y} V(q) \left[L_N\left(\frac{1}{2}q^2\ell^2\right) \right]^2$$

$$\times e^{-\frac{1}{2}q^2\ell^2 + iq_x(j_1-j_3)\frac{2\pi\ell^2}{L_y}} \delta_{q_y, \frac{2\pi(j_1-j_4)}{L_y}} \delta_{j_1+j_2, j_3+j_4}, \quad (3)$$

where $L_N(z)$ is the Nth-order Laguerre polynomial and $q^2 = q_x^2 + q_y^2$. $V(q)$ is the Fourier transformation of the electron-electron interaction:

$$V(q) = \begin{cases} \sum_m v_m L_m(q^2), \\ \frac{e^2}{\epsilon} \frac{\xi}{2} \sqrt{\pi} \exp\left(-\frac{q^2\xi^2}{8}\right) I_0\left(\frac{q^2\xi^2}{8}\right). \end{cases} \quad (4)$$

The first line describes the Haldane pseudopotential [49]. The second line is the result of modified Coulomb interaction, and $I_0(z)$ is the first kind of modified Bessel function. The factor $\delta_{j_1+j_2, j_3+j_4}$ in Eq. (3) indicates momentum conservation $j_1 + j_2 = j_3 + j_4$.

B. Operator ordering and fermionic phase

For the convenience of calculation in DMRG, we should rearrange the operator ordering in Eq. (2) and transform the fermionic operators into hard-core bosonic operators. In the sweep process of DMRG, we need to calculate the left (right) environment Hamiltonian from left (right) to right (left), thus the ordering of the operator string of some local operators must be ascending from left to right, i.e., the operator acts on the left site to the left of the string. For example, $\hat{c}_1^\dagger \hat{c}_6 \hat{c}_4 \hat{c}_9^\dagger$ is invalid but $-\hat{c}_1^\dagger \hat{c}_4 \hat{c}_6 \hat{c}_9^\dagger$ is valid. By imposing the ascending ordering on Eq. (2),

$$\hat{H}_I = \sum_{j_1 < j_2, j_3 < j_4} \mathcal{A}_{j_1, j_2, j_3, j_4}^N \hat{c}_{j_1}^\dagger \hat{c}_{j_2}^\dagger \hat{c}_{j_3} \hat{c}_{j_4}$$

$$= \sum_{j_1 < j_3 < j_4 < j_2} \mathcal{A}_{j_1, j_2, j_3, j_4}^N \hat{c}_{j_1}^\dagger \hat{c}_{j_3} \hat{c}_{j_4} \hat{c}_{j_2}^\dagger \left(\underset{j_1 \ j_3}{\overset{\circ \ \bullet}{\frown}} \underset{j_4 \ j_2}{\overset{\bullet \ \circ}{\frown}} \right)$$

$$+ \sum_{j_3 < j_1 < j_2 < j_4} \mathcal{A}_{j_1, j_2, j_3, j_4}^N \hat{c}_{j_3} \hat{c}_{j_1}^\dagger \hat{c}_{j_2}^\dagger \hat{c}_{j_4} \left(\underset{j_3 \ j_1}{\overset{\bullet \ \circ}{\frown}} \underset{j_2 \ j_4}{\overset{\circ \ \bullet}{\frown}} \right)$$

$$- \sum_{j_1 = j_3 < j_2 = j_4} \mathcal{A}_{j_1, j_2, j_1, j_2}^N \hat{n}_{j_1} \hat{n}_{j_2}, \quad (5)$$

where $\mathcal{A}_{j_1, j_2, j_3, j_4}^N = (2A_{j_1, j_2, j_3, j_4}^N - 2A_{j_2, j_1, j_3, j_4}^N)$.

Finally, we use the Jordan-Wigner transformation to transform a fermion into a hard-core boson,

$$H_I = - \sum_{j_1 < j_3 < j_4 < j_2} \mathcal{A}_{j_1, j_2, j_3, j_4}^N a_{j_1}^\dagger F_{j_1, j_4} \hat{a}_{j_3} \hat{a}_{j_4} \hat{F}_{j_4, j_2} \hat{a}_{j_2}^\dagger$$

$$- \sum_{j_3 < j_1 < j_2 < j_4} \mathcal{A}_{j_1, j_2, j_3, j_4}^N \hat{a}_{j_3} \hat{F}_{j_3, j_1} \hat{a}_{j_1}^\dagger \hat{a}_{j_2}^\dagger \hat{F}_{j_2, j_4} \hat{a}_{j_4}$$

$$- \sum_{j_1 = j_3 < j_2 = j_4} \mathcal{A}_{j_1, j_2, j_1, j_2}^N \hat{n}_{j_1} \hat{n}_{j_2}, \quad (6)$$
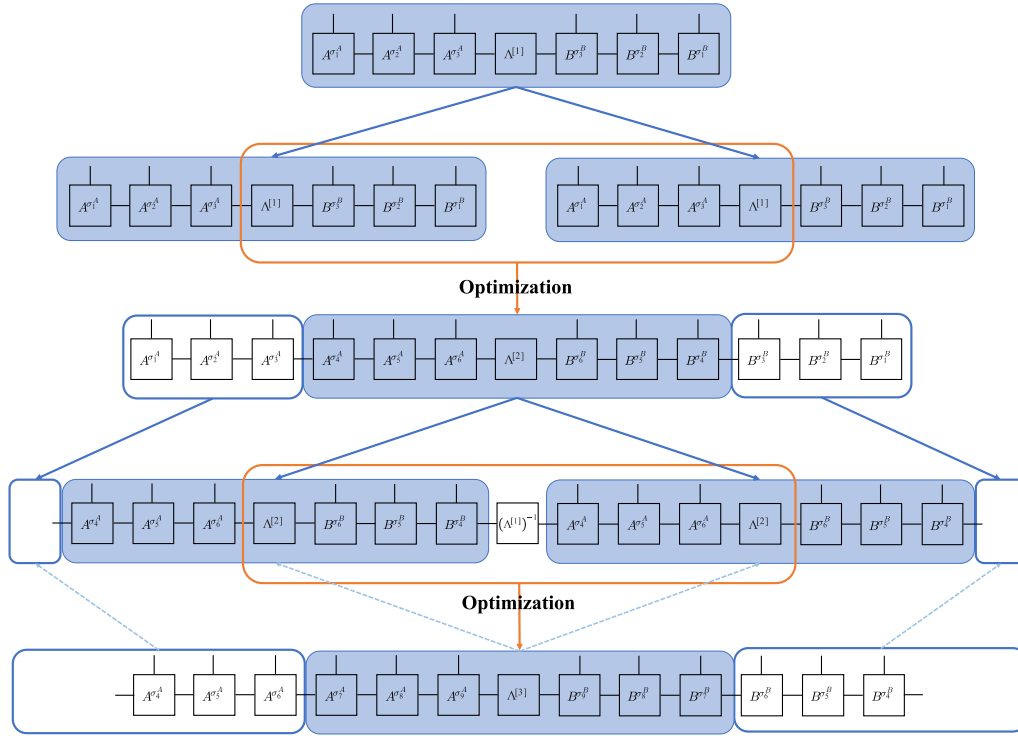
FIG. 1. *The main steps of calculating the Laughlin $\nu = 1/3$ state using iDMRG:* First line: starting from a unit cell with $2q = 6$ orbits and optimizing the energy of MPS. Second and third lines: then we enlarge the MPS by inserting a new unit cell, and we optimize the energy of this new unit cell; here we have used the initial guess. Fourth and fifth lines: by repeating the enlargement and optimization step, we can reach the thermodynamic limit and derive a translationally invariant unit cell.

where $\hat{F}_{i,j} = \Pi_{s=i+1}^{j-1} \hat{F}_s = (-1)^{\sum_{s=i+1}^{j-1} \hat{n}_s}$ is the Jordan-Wigner string operator (fermionic phase operator), and $\hat{a}^\dagger$ ($\hat{a}$) is the hard-core bosonic operator. All operators in Eq. (6) are local, and all operator strings are in ascending ordering from left to right. Conclusively, Eq. (6) is a DMRG-friendly form of many-body Hamiltonian Eq. (2).

C. Conserved quantities

Generally speaking, the invariance of a Hamiltonian under symmetry transformation gives us conserved quantum numbers. First we need to find all symmetry groups whose Hamiltonian is invariant under the symmetric operations. Since the generators of different groups may not commute with each other, we can only use the symmetry group whose generators commute with each other. These generators and the Hamiltonian can be diagonalized simultaneously. The eigenvalues of these generators are good quantum numbers of the Hamiltonian.

First, under a global gauge transformation of Landau level $\psi_{N,j} \to e^{i\theta}\psi_{N,j}$, which is the U(1) group, the Hamiltonian is invariant under this global gauge transformation. The conserve quantity corresponding to this symmetry is the particle number $[\hat{N}_e, \hat{H}] = 0$, where

$$\hat{N}_e = \sum_{j=1}^{N_\phi} \hat{n}_j = \sum_{j=1}^{N_\phi} \hat{c}_j^\dagger \hat{c}_j. \tag{7}$$

Second, we consider the translation operator $\hat{T}(\boldsymbol{a})$ [50],

$$\hat{T}(\boldsymbol{a}) = \prod_{i=1}^{N_e} \hat{T}_i(\boldsymbol{a}) = \prod_{i=1}^{N_e} \exp\left(\frac{i}{\hbar}\boldsymbol{a} \cdot \hat{\boldsymbol{K}}_i\right), \tag{8}$$

where $\hat{\boldsymbol{K}}_i = \hat{\boldsymbol{\Pi}}_i - |e|\boldsymbol{B} \times \hat{\boldsymbol{r}}_i$ ($\hat{\boldsymbol{r}}_i$ is the coordinate operator of the ith single particle) is called guiding center momentum, and $\hat{\boldsymbol{\Pi}}_i = \hat{\boldsymbol{p}}_i + |e|\boldsymbol{A}$ is canonical momentum. $\hat{K}_{i,y} = \hat{p}_{i,y}$ and $\hat{K}_{i,x} = \hat{p}_{i,x} - \frac{\hbar}{\ell^2}\hat{y}_i$, where the second subscript denotes the component of the vector. One can prove that $[\hat{T}(\boldsymbol{a}), \hat{H}] = 0$ [50,51]. Crucially, the translation operators along different directions do not commute with each other, as can be seen from the following relation:

$$[\hat{K}_{i,x}, \hat{K}_{j,y}] = i\hbar|e|B_z\delta_{ij} = -i\frac{\hbar^2}{\ell^2}\delta_{ij}. \tag{9}$$

Since our setup of the cylinder is periodic along the y-direction, we have $\hat{T}(a\boldsymbol{e}_y)\psi_{N,j}(x, y) = \psi_{N,j}(x, y + a) = e^{i\frac{2\pi j}{L_y}a}\psi_{N,j}(x, y)$, which leads to the second conserved operator $\hat{K}_y = \sum_{i=1}^{N_e} \hat{K}_{i,y}$:

$$\hat{K}_y|j_1 \cdots j_{N_e}\rangle = \frac{2\pi\hbar}{L_y} \sum_{i=1}^{N_e} j_i|j_1 \cdots j_{N_e}\rangle. \tag{10}$$
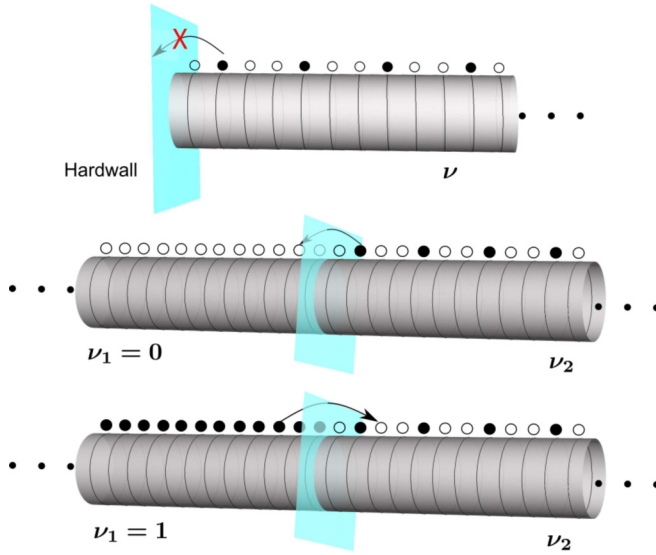
FIG. 2. *The construction of the interface:* Top: the schematic diagram of constructing the "hardwall edge," where we just drop the left boundary. Middle and bottom: the construction of the interface between two different QH states. We first cut each of the two infinite cylinders into two halves, and we glue the left half of the ν_1 state and the right half of the ν_2 state together. The blue plane denotes the interface.

Thus, the conserved quantity is

$$\langle \hat{K}_y \rangle = \frac{2\pi \hbar}{L_y} \sum_{i=1}^{N_e} j_i. \tag{11}$$

There is another definition of momentum,

$$\left\langle \frac{L_y}{2\pi \hbar} \hat{K}_y \right\rangle = \sum_{i=1}^{N_e} j_i, \tag{12}$$

which is convenient in the DMRG routine. These two definitions only differ by a constant. Unless otherwise specified, we choose the second definition in this paper.

Finally, we consider how the operator $\hat{T}(a e_x)$ affects the momentum $\hat{K}_y$. The special translation distances $X_m = \frac{2\pi \ell^2}{L_y} m (m \in \mathbb{Z})$ along the x-direction, which translate one single orbital to another, are important in the DMRG algorithm, and these operators $\hat{T}_m = \hat{T}(-X_m e_x)$ act on a single orbit,

$$\hat{T}_m \psi_{N,j}(x, y) = \psi_{N,j}(x - X_m, y) = \psi_{N,j+m}(x, y). \tag{13}$$

The momentum of this single orbit changes from j to $j + m$, which can also be seen by considering

$$\hat{T}_m^\dagger \hat{K}_y \hat{T}_m = \hat{K}_y + \frac{2\pi \hbar}{L_y} m \hat{N}_e. \tag{14}$$

Equation (14) is an important relation in some situations of the DMRG algorithm.

D. DMRG algorithm

Due to the complexity of FQH systems, the exact diagonalization (ED) research is too difficult to extend to large system sizes. In this work, to reach large sizes and discuss
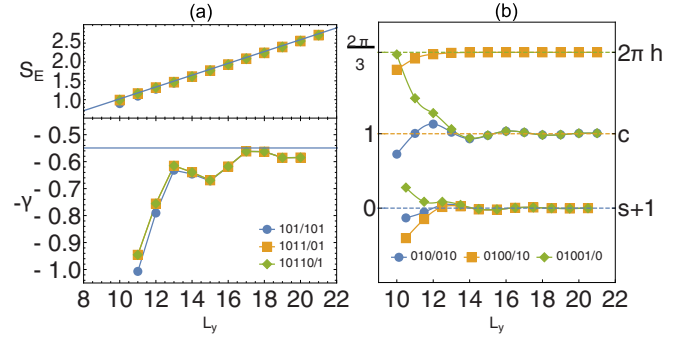

FIG. 3. *The topological order of the Laughlin 1/3 state for Coulomb interaction:* (a) The entanglement entropy of the Laughlin 1/3 state in different L_y. The upper panel is the scaling behavior of entanglement entropy $S_E \approx 0.157 L_y - \gamma$. The lower panel is the topological entanglement entropy γ where the blue horizontal line is $-\gamma = -\ln\sqrt{3}$. (b) The momentum polarization of the Laughlin 1/3 state in different L_y. The obtained topological characters are guiding center spin $s \approx -1$, topological spin $h \approx \frac{1}{3}$, and central charge $c \approx 1$.

the edge and interface physics, we will rely on the density-matrix renormalization group (DMRG) method. The DMRG algorithm [52,53] is a powerful technique for studying one-dimensional (1D) systems. For the short-range correlation length of a gapped ground state, one can truncate the Hilbert space to small dimension with high accuracy. In this section, we will illustrate the implementation of the DMRG algorithm in a FQH system [45,48,54,55]. All algorithms in this paper are implemented based on the ITensor library 3(C++ version) [56].

1. Finite DMRG

Finite DMRG (fDMRG) is a variational method to find the ground state of a system on a given finite size. First we give an initial state in the form of a matrix product state (MPS); the goal is to find the ground state of Eq. (6). Due to the incompressible natural of the FQH state, the correlation and entanglement are finite for the ground state. Thus, we can truncate the MPS by diagonalizing the reduced density matrix (or singular value decomposition for the MPS, i.e., SVD) and keep the largest D eigenstates and eigenvalues (or singular values, the square root of eigenvalues), where D is called the bond dimension of the MPS, and the summation of all discarded eigenvalues is called the truncation error ϵ. In the limit $D \rightarrow \infty$, the truncation error becomes zero and the MPS representations become exact. We will discuss the convergence of fDMRG in Sec. II D 2.

Since the Hamiltonian Eq. (6) commutes with $\hat{T}(a e_y)$, the momentum of the initial state is invariant in fDMRG, so we can only reach a ground state with the same momentum as the initial state. This provides a way to select or control the ground state by starting from an initial state with specific momentum. For instance, for the Laughlin $\nu = 1/3$ state, the root configuration is $|010010010\cdots\rangle$, and the model ground state is a superposition of $|010010010\cdots\rangle$ and its "squeeze" sequences (such as $|001100010\cdots\rangle$, $|001010100\cdots\rangle\cdots$) [57]. Note that the third line of Eq. (5) actually describes a typical
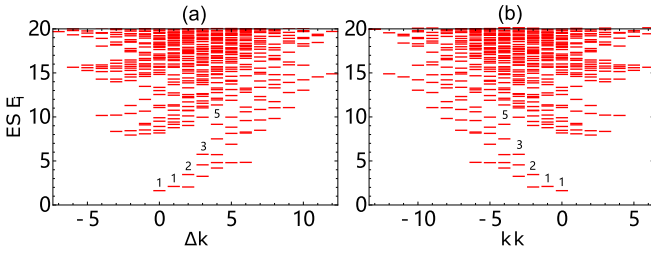
FIG. 4. *The ES of the $\nu = 1/3$, $2/3$ state for Coulomb interaction:* The entanglement spectra of (a) Laughlin $1/3$ state and (b) $2/3$ state. The circumference is $L_y = 20\ell$. Both show the typical U(1) counting $1, 1, 2, 3, 5, \ldots$, but their chirality is opposite.

"squeeze," and therefore we have the possibility to reach the ground state in fDMRG.

In this paragraph, we illustrate the basic concept of "root configuration." The "root configuration" is related to the generalized Pauli exclusion principle. For example, the generalized Pauli exclusion principle of the Laughlin $\nu = 1/3$ state is that there is no more than one particle in three consecutive orbits; the representation in the second quantization language $|010010 \cdots\rangle$ is called the "root configuration." One may ask, why not $|100100 \cdots\rangle$ or $|001001 \cdots\rangle$? The answer is that these two states are also the Laughlin $\nu = 1/3$ state, but they carry a pair of quasiparticle and quasihole excitation at both ends of the cylinder (see Appendix C). As we explained above, the "squeezing" operators preserve the momentum quantum number, and we can use the "root configuration" to represent the ground state in this momentum space.

2. Improvement of DMRG

In this subsection, we will discuss some techniques of DMRG in solving the ground state of Eq. (6). These tricks are important for DMRG in FQH systems, or DMRG in momentum space. To proceed, let us briefly explain why we highlight these techniques. Let us consider the simplest Hamiltonian with only a nearest-neighbor interaction (e.g., $\hat{S}_i \cdot \hat{S}_{i+1}$, $\hat{c}_i^\dagger \hat{c}_{i+1}$); the two-site DMRG can find an optimal state even if the initial state is a product state. The two-site DMRG can only "see" the nearest-neighbor interaction, i.e., it can only find the local optimal wave function in the two-site Hilbert space, for example $\mathcal{H}_2 = \text{span}(|00\rangle, |10\rangle, |01\rangle, |11\rangle)$. Once we give a product state like $|010010 \cdots\rangle$, the momentum conservation prohibits the nearest-neighbor hopping, hence the initial state $|010010 \cdots\rangle$ never changes, and the DMRG algorithm will fall into a local solution forever.

Because of this limitation, we list some methods here to overcome this drawback of the two-site DMRG:

n-site DMRG. Since the momentum conservation prohibits nearest-neighbor hopping and the simplest "squeeze" step ($|1001\rangle \rightarrow |0110\rangle$)) requires at least 4-site optimization. The most straightforward way is to use *n-site* optimization instead of 2-site. The *n-site* algorithm for some $n > 2$ depends on the filling [45]. This significantly increases the memory requirements of the algorithm.

Superposition initial state. The 2-site update cannot reach the optimal state from the initial state $|010010 \cdots\rangle$. Since the
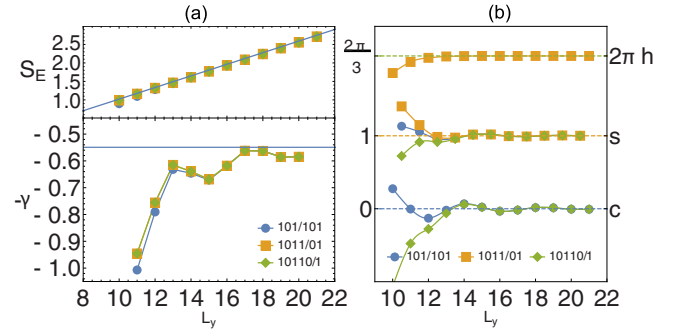

FIG. 5. *The topological order of the $2/3$ state for Coulomb interaction:* (a) The entanglement entropy of the $2/3$ state in different L_y. The upper panel is the scaling behavior of entanglement entropy $S_E \approx 0.157 L_y - \gamma$. The lower panel is the topological entanglement entropy γ, where the blue horizontal line is $-\gamma = -\ln\sqrt{3}$. (b) The momentum polarization of the $2/3$ state in different L_y. The obtained topological characters are guiding-center spin $s \approx 1$, topological spin $h \approx \frac{1}{3}$, and chiral central charge $c \approx 0$.

model state is a superposition of the root configuration and its "squeeze," we can use the superposition of a set of "squeezed" states instead of a product state [54].

Global subspace expansion. Global subspace expansion (GSE) is proposed by Ref. [58], which is used to improve the traditional time-dependent variational principle (TDVP) algorithm and avoid falling into local solutions. The key idea of GSE is the enlargement of tangent space by Krylov subspace of order k,

$$\mathcal{K}(\hat{H}, |\psi\rangle) = \text{span}\{|\psi\rangle, \hat{H}|\psi\rangle, \ldots, \hat{H}^{k-1}|\psi\rangle\}, \quad (15)$$

and to use the state in this Krylov subspace instead of $|\psi\rangle$.

Density matrix correction. Density matrix correction [59] can improve the convergence dramatically. The main idea is illustrated as follows. Equation (6) can be written as $\hat{H} = \sum_i \hat{H}_{L,i} \otimes \hat{H}_{R,i}$ and $|\psi\rangle = \sum_i s_i |L_i\rangle \otimes |R_i\rangle$. The reduced density matrix correction is to add the corrected term $\Delta\rho = \sum_i \langle R_i|\psi'\rangle\langle\psi'|R_i\rangle$ to the original reduced density matrix $\rho = \sum_i \langle R_i|\psi\rangle\langle\psi|R_i\rangle$, where $|\psi'\rangle = \sum_i \hat{H}_{L,i} \otimes \hat{I}_R|\psi\rangle$. The final step is to replace the original reduced density matrix ρ with the new one, $\rho + \delta\Delta\rho$, where δ is a small controllable weight constant. Sometimes $\Delta\rho$ is regarded as a "noise" term, and then δ is the intensity of "noise."

Lastly, when applying finite DMRG to the cylinder geometry, to avoid the electrons becoming trapped at the two ends of the finite cylinder, it is necessary to include an additional trap potential [60]. The selection of trap potential is usually empirical. An alternative way to overcome this issue is to work on the infinite cylinder geometry, as discussed below.

3. Infinity DMRG

Infinity-DMRG (iDMRG) is a powerful method for the FQH systems [45]. In this subsection, we will discuss the technical details for implementing iDMRG in FQH systems. We choose the Laughlin $\nu = 1/3$ state as an example, and we show the main process of iDMRG in Fig. 1.

Step 1: Starting from a unit cell with $2q = 6$ orbits, using the fDMRG method to minimize the energy, we have the
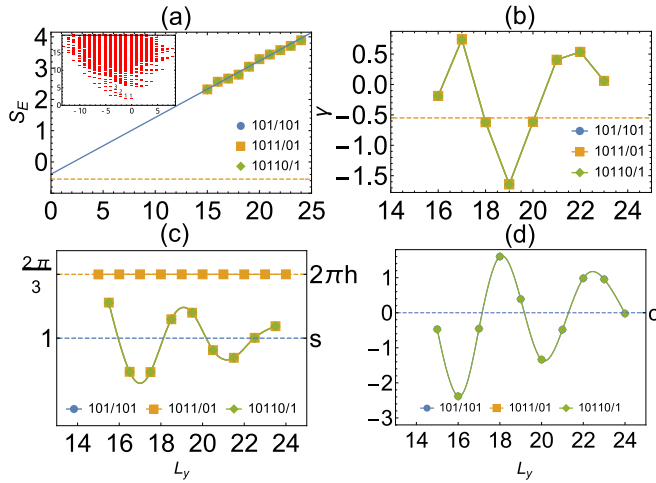
FIG. 6. *The topological characters of the $\nu = 8/3$ state for Coulomb interaction:* (a) The EE and (b) the extracted TEE of the $\nu = 8/3$ state; the yellow dashed line is $-\ln\sqrt{3}$. (c),(d) The momentum polarization of the $\nu = 8/3$ state in different L_y. Part (c) shows the extracted topological spin h_a and guiding-center spin s, while (d) is the central charge c.

ground-state MPS:

$$|\psi_1\rangle = \sum_\sigma A^{\sigma_1^A} A^{\sigma_2^A} A^{\sigma_3^A} \Lambda^{[1]} B^{\sigma_3^B} B^{\sigma_2^B} B^{\sigma_1^B} |\sigma\rangle, \qquad (16)$$

where A^σ and B^σ are left-orthogonal and right-orthogonal tensors, respectively.

Step 2: After the first step, we insert a new unit cell into the center of the original MPS. Following the intuition of MPS, we write down the "enlarged" MPS as

$$|\psi_2\rangle = \sum_\sigma L\big(A^{\sigma_4^A} A^{\sigma_5^A} A^{\sigma_6^A} \Lambda^{[2]} B^{\sigma_6^B} B^{\sigma_5^B} B^{\sigma_4^B}\big) R|\sigma\rangle, \qquad (17)$$

where $L = A^{\sigma_1^A} A^{\sigma_2^A} A^{\sigma_3^A}$ and $R = B^{\sigma_3^B} B^{\sigma_2^B} B^{\sigma_1^B}$. The crucial task is to find a good initial guess for the newly inserted tensors which can help to quickly reach the translationally invariant state in the calculation. Following the key ideas in Ref. [53], the good initial guess is intended to translate the right half (including the tensor containing singular values) of Eq. (16) to the left half of the newly inserted unit cell, and vice versa for the other half. Therefore, the initial guess can be written as

$$|\psi_2\rangle = \sum_\sigma L\big(\Lambda^{[1]} B^{\sigma_3^B} B^{\sigma_2^B} B^{\sigma_1^B} A^{\sigma_1^A} A^{\sigma_2^A} A^{\sigma_3^A} \Lambda^{[1]}\big) R|\sigma\rangle. \qquad (18)$$

It is worth noting that we have translated the tensors in this step; the conserved quantities of each tensor need to be treated carefully. Since the generators of translation operators do not commute with each other, translating tensors in MPS will change the quantum numbers they carried. Following Eq. (14), when we translate $A(B)$ and Λ from position i to j, the quantum numbers must change from (N_e, K) to $(N_e, K + (j-i)N_e)$.

Step 3: Optimizing the newly inserted unit cell by fDMRG and keeping the other tensors unchanged, we get the following

MPS with 12 orbits:

$$|\psi_2\rangle = \sum_\sigma L\big(A^{\sigma_4^A} A^{\sigma_5^A} A^{\sigma_6^A} \Lambda^{[2]} B^{\sigma_6^B} B^{\sigma_5^B} B^{\sigma_4^B}\big) R|\sigma\rangle. \qquad (19)$$

Step 4: Using the same method to insert a new unit cell into the middle again,

$$|\psi_3\rangle = \sum_\sigma L\big(\Lambda^{[2]} B^{\sigma_6^B} B^{\sigma_5^B} B^{\sigma_4^B} (\Lambda^{[1]})^{-1} A^{\sigma_4^A} A^{\sigma_5^A} A^{\sigma_6^A} \Lambda^{[2]}\big) R|\sigma\rangle, \qquad (20)$$

where $L = A^{\sigma_1^A} A^{\sigma_2^A} A^{\sigma_3^A} A^{\sigma_4^A} A^{\sigma_5^A} A^{\sigma_6^A}$ and $R = B^{\sigma_6^B} B^{\sigma_5^B} B^{\sigma_4^B} B^{\sigma_3^B} B^{\sigma_2^B} B^{\sigma_1^B}$. By repeating *Step 3* and *Step 4*, we can reach the thermodynamic limit and derive a translationally invariant unit cell.

E. Construction of the interface

In this paper, we will investigate the interface physics of FQH states. This is partially motivated by recent experimental works (e.g., Ref. [13]). In preview works [61–63], the interface can be constructed through 2D conformal field theory. In this work, we provide another way to build the interface by optimizing the MPS energy in the DMRG algorithm. Now we explain the "cut-and-glue" scheme in which we construct the interface of FQH states. The general steps are as follows: (i) After the iDMRG algorithm converges, we get the translation-invariant MPS unit cell, and we cut the MPS into two halves, i.e., the left part and the right part. (ii) We drop the one part (say the left one) and project the bond between the left boundary and the first orbit of the right part to the state that has the same quantum number as the root configuration. (iii) Now we have a semi-infinite cylinder with a filling factor ν_1, and then we glue it together with another semi-infinite cylinder with a filling factor ν_2; see Fig. 2. (iv) We optimize the energy of MPS around the interface region and find the lowest energy configuration, as with the usual finite DMRG procedure.

In this paper, we will construct three types of interfaces (we will use "$\nu_1|\nu_2$ interface" to denote the interface between the ν_1 state and the ν_2 state):

(i) The first one is called the "hardwall edge" (or with a sharp cleaved edge) [64], where the electron cannot enter the hardwall, or it can be seen as a situation in which the other half takes an infinite (sharp) confining potential [see Fig. 2 (top)]. In this case, after we cut the translation-invariant MPS into two halves, we can directly optimize the semi-infinite cylinder by skipping the glue step.

(ii) The second type is to glue together an integer quantum Hall state with filling ν_1 and the FQH ν_2 state, where ν_1 is smaller than ν_2 [see Fig. 2 (middle)]. For example, for the $\nu_1 = 0|\nu_2 = 2/3$ or $\nu_1 = 2|\nu_2 = 8/3$ interface, the integer quantum Hall half is used to gap out the integer edge modes of the FQH half. Please note that in this case, the electron could enter the integer filling region, in contrast to the "hardwall edge."

(iii) The third type is similar to the second, but ν_1 is greater than ν_2 [see Fig. 2 (bottom)], for example $\nu_1 = 1|\nu_2 = 2/3$ or $\nu_1 = 3|\nu_2 = 8/3$. In this case, tunneling through the interface is allowed.

Finally, we stress that this construction scheme has many advantages. First, the construction is based on the iDMRG scheme in cylinder geometry [45], so that we can get a target
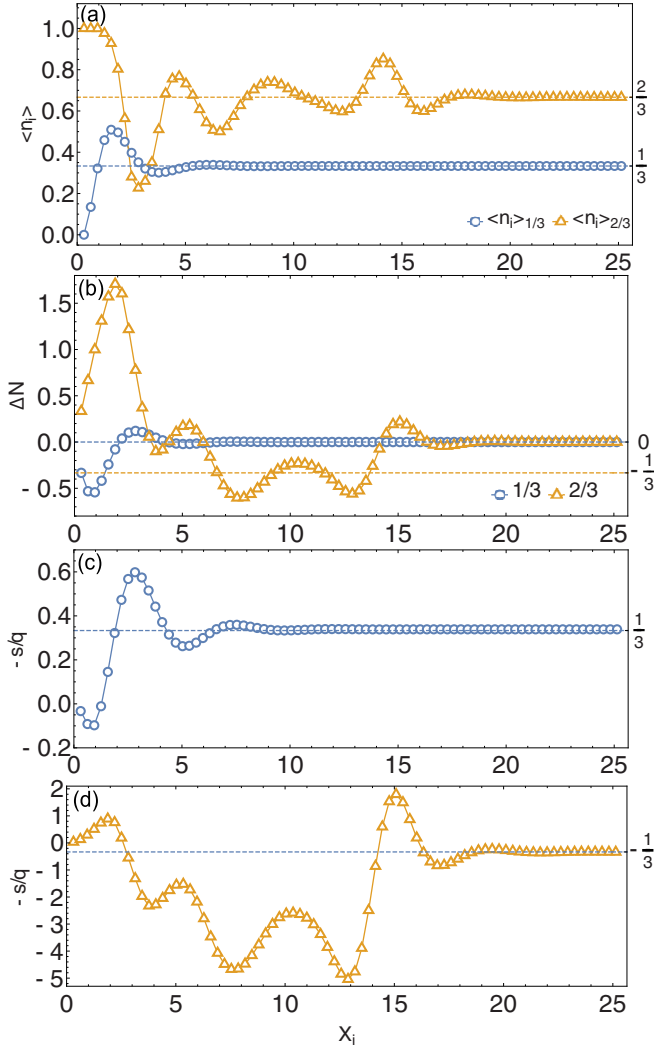
FIG. 7. *The edge of the $\nu = 1/3$, $2/3$ state:* (a) The density profile and (b) the integral of the Laughlin $1/3$ state (blue labels) and the $2/3$ state (yellow labels). (c),(d) The extracted guiding-center spin from the dipole moment, where (c) for the Laughlin $1/3$ state and (d) for the $2/3$ state. We can see that the quantity $-s/q$ converges to $1/3$ and $-1/3$ for the Laughlin $\nu = 1/3$ state and $\nu = 2/3$ state, respectively. Here, we choose the Haldane pseudopotential $v_1 = 1.0$ and the circumference of the cylinder, $L_y = 20\ell$.

FQH state in an unbiased way, without any empirical information such as the confining potentials or the background charge layer. Second, after the gluing step we perform an energetically variational optimization, so the obtained configurations (shown below) on the interface are the lowest energy configuration. Next, this scheme will be displayed to investigate edges and interfaces in greater detail.

F. Topological characters in the bulk and on the interface

In this section, we summarize the physical quantities that we will utilize for identifying the topological properties in the bulk and on the interface. They include entanglement spectra for the chiral edge state, topological entanglement entropy for the quasiparticle quantum dimension, momentum
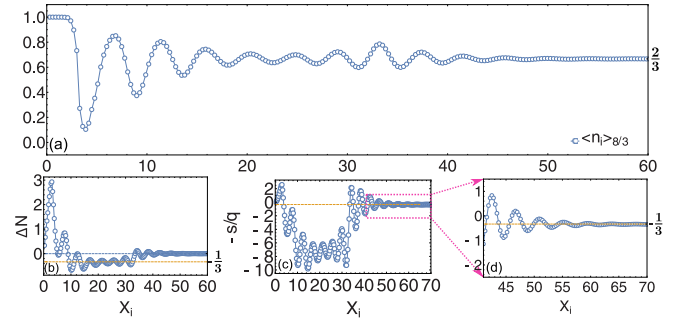

FIG. 8. *The "hardwall edge" of the $\nu = 8/3$ state:* (a) The density profile and (b) integral of the $\nu = 8/3$ state. (c) The guiding-center spin extracted from the dipole moment. (d) A zoomed portion of (c), in which we can clearly see that $-s/q$ converges perfectly to $-1/3$ as the theoretical prediction. Here, we choose Coulomb interaction and the circumference $L_y = 21$.

polarization for topological spin and guiding-center spin, and electric dipole momentum for guiding-center spin.

1. Entanglement spectra

FQH states are gapped in the bulk but contain gapless edge excitation. This means that the electrons in bulk are localized, and the transport properties (electrical and thermal conductance) [65–70] are determined by the gapless edge states, which are extended. This implies that there is a certain connection between edge and bulk states. On the other hand, the topological order of a FQH state can be determined by its edge states [4]. Moreover, the entanglement spectrum of a FQH wave function can be seen as some special "energy levels" which correspond to the entanglement Hamiltonian $\hat{\mathcal{H}}_E$. It has been shown [71,72] that there is a general relationship between the entanglement spectrum and the edge state spectrum of topological quantum states. Thus, one can investigate the entanglement spectra of a FQH state instead of the true edge excitation, which provides a straightforward way to study the edge excitation. We briefly describe the method of calculating the entanglement spectra below.

Once we get the ground-state wave function $|\psi\rangle$, consider a bipartition of the system into two parts A and B, and the Hilbert space $H = H_A \otimes H_B$. One can write $|\psi\rangle$ as a superposition of some product states $|\psi\rangle = \sum_{i,j} c_{i,j} |\psi_i^A\rangle \otimes |\psi_j^B\rangle$, where $|\psi_i^A\rangle \in H_A$ and $|\psi_j^B\rangle \in H_B$. By employing the Schmidt decomposition (SVD), $|\psi\rangle$ has a special form,

$$|\psi\rangle = \sum_i \lambda_i |\psi_i^A\rangle \otimes |\psi_i^B\rangle, \tag{21}$$

where $\lambda_i = \exp\left(-\frac{1}{2}\xi_i\right) \geqslant 0$, and ξ_i's can be seen as "energy levels" [72]. One can write the reduced density matrix as $\hat{\rho}_A = \mathrm{tr}_B |\psi\rangle\langle\psi| = \sum_i \exp\left(-\xi_i\right)|\psi_i^A\rangle\langle\psi_i^A|$, which is diagonal, thus we can see ξ_i as eigenvalues of $\hat{\mathcal{H}}_E = -\ln(\hat{\rho}_A) = \sum_i \xi_i |\psi_i^A\rangle\langle\psi_i^A|$, where $\hat{\mathcal{H}}_E$ is called the "entanglement Hamiltonian" and ξ_i's are "entanglement spectra" (ES). Therefore, we can calculate the ES through $\xi_i = -\ln(\lambda_i^2)$.

The remarkable feature of ES is the low-energy excitation. For example, the $\hat{u}(1)$ free chiral boson Hamiltonian $H_e = \sum_{k>0} \epsilon(k) b_k^\dagger b_k$ is the effective Hamiltonian of the Laughlin
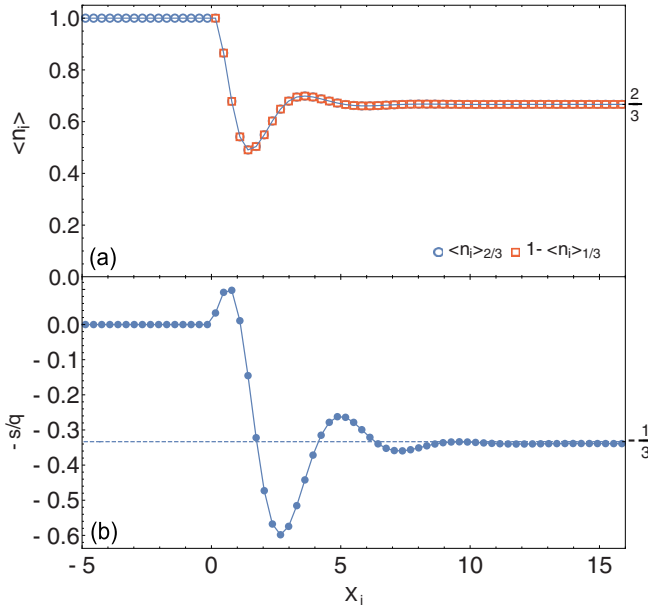
FIG. 9. *The density profile of the* $\nu = 1|\nu = 2/3$ *interface:* (a) The density profile of the $\nu = 1|\nu = 2/3$ interface (blue circle). The red square is $1 - \langle \hat{n}_i \rangle_{1/3}$, where $\langle \hat{n}_i \rangle_{1/3}$ is the density of the Laughlin $\nu = 1/3$ state in Fig. 7(a). Here, we see the $\nu = 1|\nu = 2/3$ interface is equivalent to a hole-type Laughlin 1/3 state embedded in the integer quantum Hall $\nu = 1$ background. (b) The extracted guiding center spin from the dipole moment of the $\nu = 1|\nu = 2/3$ interface; the results converge to $-1/3$ perfectly as X_j increases, where $-s/q = -1/3$ is the theoretical prediction.

state, and the counting of low-energy excitation obeys [4]

$$\Delta k: \quad 0 \quad 1 \quad 2 \quad 3 \quad 4 \quad 5 \quad 6 \cdots,$$
$$\text{Degeneracy}: \quad 1 \quad 1 \quad 2 \quad 3 \quad 5 \quad 7 \quad 11 \cdots.$$

Alternatively, the typical counting "1, 1, 2, 3, 5, 7 . . ." in the ES tells us that the effective edge theory is described by $\hat{u}(1)$ free chiral boson theory.

2. Area law and topological entanglement entropy

A prominent measure of the entanglement between one part and the rest of a quantum many-body system is entanglement entropy (EE) [73]. The Neumann entropy $S_E = -\text{tr}(\hat{\rho}_A \ln \hat{\rho}_A)$ of the reduced density matrix $\hat{\rho}_A = \sum_i \exp(-\xi_i)|\psi_i^A\rangle\langle\psi_i^A|$ is

$$S_E = -\sum_i \lambda_i^2 \ln \lambda_i^2 = \sum_i \xi_i \exp(-\xi_i). \quad (22)$$

Generally, for a gapped state, the EE S_E obeys the "area law," which means the EE is proportional to the "area" of the joint boundary. Importantly, in addition to the area law, there is an emergent nonzero constant term for the topologically ordered states, called topological entanglement entropy (TEE) [74,75].

Now, we focus on the FQH states on a cylinder. When we cut the cylinder along the periodic direction, the area of the joint boundary is the circumference $L_y = L$, and the EE of a FQH state scales as [76]

$$S_E = \alpha L - \gamma_a + O(1/L), \quad (23)$$

where γ_a is TEE and α is a nonuniversal constant. The TEE γ_a is a topological quantity that can be used to determine the topological order, and it has a theoretical value $\gamma_a = \ln(\mathcal{D}/d_a)$, where d_a is the quantum dimension of anyon a, and $\mathcal{D} = \sqrt{\sum_a d_a^2}$ [75] is the total quantum dimension of its topological field theory.

3. Momentum polarization

Following Ref. [46], the topologically ordered state on a cylinder corresponds to the topological quasiparticle on each side. In addition, the rotation along the periodic direction will not give us any information due to the rotational invariance of the cylinder. If one can rotate one side and keep another side unchanged, this progress will give us a phase that contains information of the quasiparticle on this side. This idea can be realized by dividing the cylinder into two parts along the periodic direction. We denote these two parts as A and B, and we apply the operator $\hat{T}_y^A$ to the A part, where $\hat{T}_y^A$ is the restriction of Eq. (8),

$$\hat{T}_y^A = \prod_{i \in A} \exp\left(\frac{i}{\hbar}L_y\hat{K}_{i,y}\right). \quad (24)$$

We obtain the phase

$$\exp(i2\pi\langle M\rangle_a) = \langle\psi_a|\hat{T}_y^A|\psi_a\rangle = \text{tr}_A(\hat{\rho}_A\hat{T}_y^A), \quad (25)$$

where $|\psi_a\rangle$ denotes the ground state corresponding to the topological sector a. Since $\hat{T}_y^A$ commutes with the Hamiltonian, we can diagonalize $\hat{\rho}_A$ and $\hat{T}_y^A$ simultaneously. We can calculate $\langle M\rangle_a$ from ES by

$$\langle M\rangle_a = \text{tr}_A\left(\hat{\rho}_A \frac{L_y}{2\pi\hbar}\hat{K}_{A,y}\right) = \sum_i e^{-\xi_i}\left\langle\frac{L_y}{2\pi\hbar}\hat{K}_{A,y}\right\rangle_i, \quad (26)$$

where $\hat{K}_{A,y} = \sum_{i \in A} \hat{K}_{i,y}$ is the guiding center momentum operator in the A part, and $\langle\hat{O}\rangle_i = \langle\psi_i^A|\hat{O}|\psi_i^A\rangle$. This phase $\langle M\rangle_a$ contains three important topological quantities,

$$\langle M\rangle_a - \langle M\rangle_{\text{root}} = \frac{\eta^g}{2\pi\hbar}L_y^2 - h_a + \frac{c - \nu}{24}, \quad (27)$$

where $\eta^g = -\frac{\hbar}{4\pi\ell^2}\frac{s}{q}$ is the guiding-center Hall viscosity [77] and s is the guiding-center spin [47,78–80]. The subscript "root" in $\langle M\rangle_{\text{root}}$ means that this term is calculated using the root state $|\psi_{\text{root}}\rangle$ [47]. The second term h_a is the topological spin corresponding to quasiparticle a [45,46], and c is the central charge of the underlying edge conformal field theory (CFT). The last term $\nu = p/q$ is the filling factor of a FQH state. These three quantities s, h_a, c provide rich topological information. First, s is a quantized quantity corresponding to the nondissipative response of the metric perturbation [81], similar to how the Hall conductance is the response of electromagnetic gauge A. The other two quantities h_a and c are elements of the modular-$\mathcal{T}$ matrix, which is the unitary transformation of the ground-state manifold under modular transformation. Moreover, the modular matrix can be used to describe the topological order [82].

4. Electric dipole moment and guiding-center spin

Near the edge or around the interface, the intrinsic or external electric field inevitably induces a nonuniform
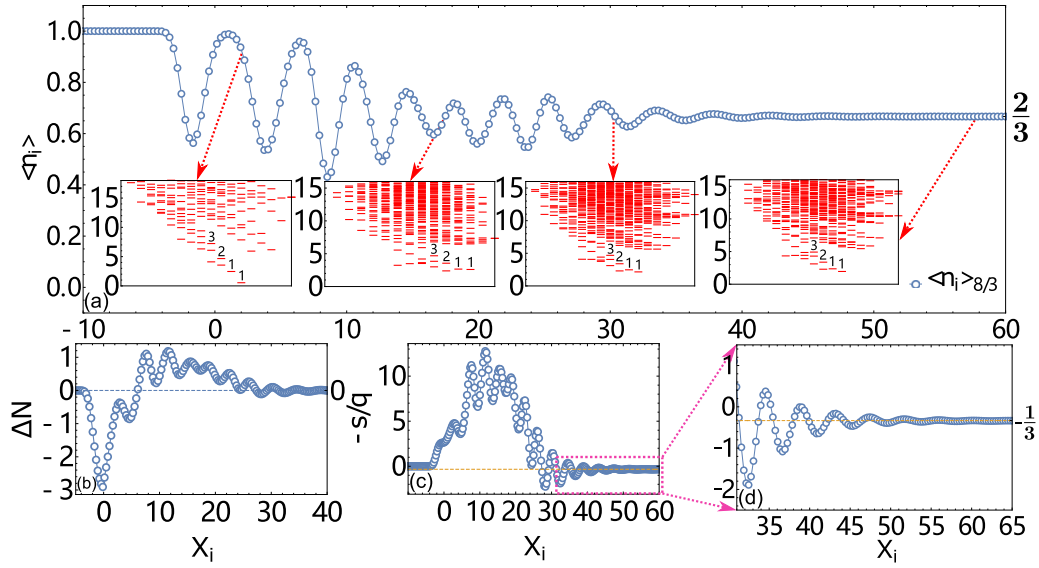
FIG. 10. *The $\nu = 3 | \nu = 8/3$ interface:* (a) The density profile of the $\nu = 3 | \nu = 8/3$ interface. The left half ($X_j < 0$) is the $\nu = 3$ ($\nu = 1$ in the SLL) IQH state, and the right ($X_j > 0$) is $\nu = 8/3$ ($\nu = 2/3$ in the SLL). The insets show the ES in different positions; they all exhibit the same chirality. (b) The density integral of this interface. (c) The guiding-center spin extracted from the dipole moment. (d) A zoomed portion of (c); we can clearly see that $-s/q$ converges perfectly to $-1/3$ as the theoretical prediction. Here, we choose Coulomb interaction and the circumference $L_y = 21$.

density distribution of electrons. One typical result is that the chiral edge mode forms and propagates along the edge or interface. Recently, it has been realized that the nonuniform density distribution gives a quantized dipole moment, which is connected to the finite Hall viscosity of FQH liquids [47], and it has been numerically verified in several systems [47,83].

To be specific, the intrinsic dipole moment coupled to the electric field generates an electric force. This electric force counterbalances the viscous force applied on the edge modes, which gives the relation [47]

$$\eta^g = \frac{p_y}{L_y} B_z = -\frac{p_y}{L_y} B, \tag{28}$$

where B is the magnetic field, $\eta^g = -\frac{\hbar}{4\pi \ell^2} \frac{s}{q}$ is the guiding-center Hall viscosity, and p_y is the dipole moment

$$p_y = -\frac{2\pi |e|}{L_y} \sum_i (\langle \hat{n}_i \rangle - \nu) i. \tag{29}$$

Now we have

$$-\frac{s}{q} = \frac{8\pi^2}{L_y^2} \sum_i (\langle \hat{n}_i \rangle - \nu) i, \tag{30}$$

where s is the guiding-center spin and q is the denominator of $\nu = p/q$. In the following, we will show that the dipole moment is an important quantity, even though it is calculated by the nonuniversal oscillated density (depending on the interaction), but the dipole moment (or guiding-center spin) is protected by topology; for more details, see Sec. IV and Ref. [47].

5. Relations between guiding-center spin and topological shift

Generally, the total Hall viscosity of a FQH state includes two parts:

$$\eta^H = \eta^o + \eta^g = \frac{\hbar}{4\pi \ell^2} \left(\nu \tilde{s} - \frac{s}{q} \right) = \frac{\hbar \nu}{4\pi \ell^2} \bar{s} = \frac{\hbar \nu}{8\pi \ell^2} \mathcal{S}, \tag{31}$$

where $\eta^g = -\frac{\hbar}{4\pi \ell^2} \frac{s}{q}$ is the guiding-center Hall viscosity, and $\eta_o = \frac{\hbar}{4\pi \ell^2} \nu \tilde{s}$ is the Landau-orbital Hall viscosity [47,81]. The quantity $\tilde{s} = n + \frac{1}{2}$ in η_o is the Landau-orbital spin for the nth ($n = 0, 1, 2, \dots$) Landau level. Since η_o comes from the Landau-orbital form factor and we are working on the LL-projected Hamiltonian, it does not appear in Eqs. (27) and (28). Interestingly, by defining the mean "orbital spin" $\bar{s} = \tilde{s} - \frac{s}{p}$ [80], one can relate it to the topological shift $\mathcal{S}$ [44] via $\mathcal{S} = 2\bar{s}$ [80]. From Eq. (31), we can write down the relation between guiding-center spin and topological shift,

$$\mathcal{S} = 2\left(\tilde{s} - \frac{s}{p} \right). \tag{32}$$

Equation (32) means that we can obtain a topological shift by calculating the guiding-center spin since $\tilde{s}$ is a known number. Please note, the filling factor $\nu = p/q$ in both Eqs. (31) and (32) is the filling of a single Landau level. For example, the $\nu = 8/3$ state has total filling $\nu = 2 + 2/3$, so its filling in the second Landau level is $\nu = 2/3$ and we should use $\nu = p/q = 2/3$ in Eqs. (31) and (32). If the nature belongs to the Laughlin state, $\mathcal{S}$ is 0 and 2 for the 2/3 state and the $2 + 2/3$ state, respectively. As a comparison, non-Abelian Z_4 parafermion hosts $\mathcal{S} = 3$ [40,41], and Bonderson-Slingerland hierarchy has $\mathcal{S} = 4$ [43] (in LLL). Finally, we provide some details of the theoretical derivation of $\mathcal{S}$ and s for the
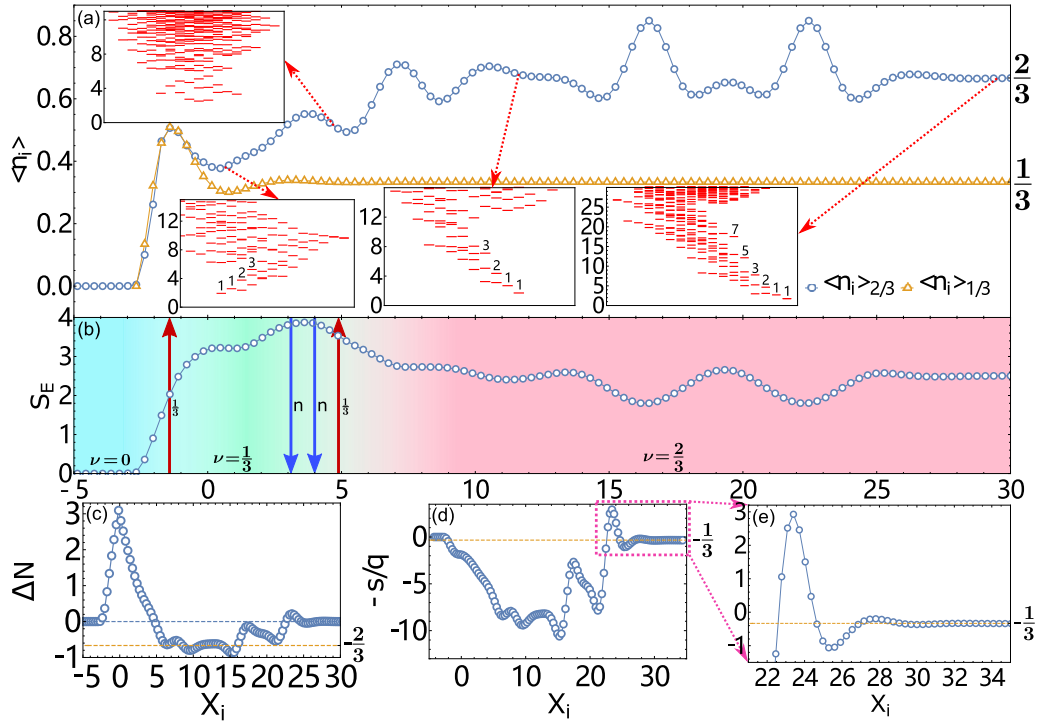
FIG. 11. *The $\nu = 0|\nu = 2/3$ interface:* (a) The density profile of the $\nu = 0|\nu = 2/3$ interface. The left half ($X_j < 0$) is the $\nu = 0$ vacuum state and the right ($X_j > 0$) is the $\nu = 2/3$ state. The insets show the ES in different positions. The ESs in regions $X_i \sim 0\ell$ and $X_i > 10\ell$ have opposite chirality, which means a small region of Laughlin 1/3 has emerged. The ESs in the upper left ($X_i \approx 4.39\ell$) have particle-hole symmetry, which is evidence of the existence of the interface between the 1/3 state and its particle-hole conjugation (2/3 state). (b) The EE of this interface, and the background is the schematic diagram of this interface; the red and blue arrows represent the 1/3 chiral boson and neutral mode, respectively. (c) The density integral of this interface. (d) The guiding-center spin extracted from the dipole moment. (e) A zoomed portion of (d). We can clearly see that $-s/q$ converges perfectly to $-1/3$ as the theoretical prediction. Here, we choose Haldane pseudopotential $v_1 = 1.0$ and the circumference $L_y = 20$.

Abelian $\nu = n + 1/q$ state and the $\nu = n + 1 - 1/q$ state in Appendix B.

6. Relations between dipole moment and momentum polarization

Now, we illustrate the relation between dipole moment and momentum polarization, which has also been explained in Ref. [47]. Starting from Eq. (26), we have $\langle M \rangle_a = \text{tr}_A(\hat{\rho}_A \frac{L_y}{2\pi\hbar} \hat{K}_{A,y})$; note that the momentum operator $\hat{K}_{A,y}$ can be expressed as $\hat{K}_{A,y} = \sum_{i \in A} \hat{n}_i \frac{2\pi i\hbar}{L_y}$. Using this relation, we have

$$\langle M \rangle_a = \sum_{i \in A} \text{tr}_A(\hat{\rho}_A \hat{n}_i) \times i = \sum_{i \in A} \langle \hat{n}_i \rangle \times i. \quad (33)$$

Comparing Eqs. (27) and (30), we can find that Eq. (30) should be

$$-\frac{s}{q} + \frac{8\pi^2}{L_y^2}\left(-h_a + \frac{c - \nu}{24}\right) = \frac{8\pi^2}{L_y^2} \sum_i (\langle \hat{n}_i \rangle - \nu)i. \quad (34)$$

Here, we have found a correction in Eq. (30) of order $O(L_y^{-2})$, which will vanish in the thermodynamic limit. Please note that the $O(L_y^{-2})$ coefficient on the right-hand side of Eq. (30) can be absorbed by $\frac{8\pi^2}{L_y^2} \sum_i i \approx \int k \, dk$, where $k = \frac{2\pi i}{L_y}$, and Eq. (34) can be written as

$$-\frac{s}{q} = \int dk(\langle \hat{n}(k) \rangle - \nu(k))k. \quad (35)$$

In Appendix C, we provide more details about the corrected term in Eq. (34).

III. TOPOLOGICAL PROPERTIES IN THE BULK

In this section, we will study the bulk properties of the $\nu = 1/3, 2/3$ states. The nature of the $\nu = 2/3$ state is thought to be the particle-hole conjugation of the Laughlin $\nu = 1/3$ state [84,85], but the discussion on the $\nu = 2/3$ state has recently been revived [36,37,39], mainly due to the experimental identification of complex edge structures that are beyond the previous description [9–11]. We also study the $\nu = 2/3$ state in the second Landau level (SLL), i.e., the $\nu = 8/3$ state. It has been theoretically proposed that this state could be non-Abelian. These are the motivations for this work.

Here, we list the values of the parameters we used in iDMRG. (a) We choose a cutoff $\epsilon_H = 10^{-6}$ of a Hamiltonian, which means that we only consider terms with coefficients in Eq. (3) $|A^N_{j_1,j_2,j_3,j_4}| \geqslant \epsilon_H$. (b) The upper bound of truncation error in DMRG is chosen to be $\epsilon_D = 10^{-7}$ and the bond dimension of MPS is automatically increased to ensure that the truncation error is smaller than ϵ_D. (c) The intensity of noise in the density matrix correction is $\delta \approx 10^{-3}$–10^{-4}. (d) The regulated length in the Coulomb interaction is $\xi = 4\ell$. The full text will use the above setting of parameters.
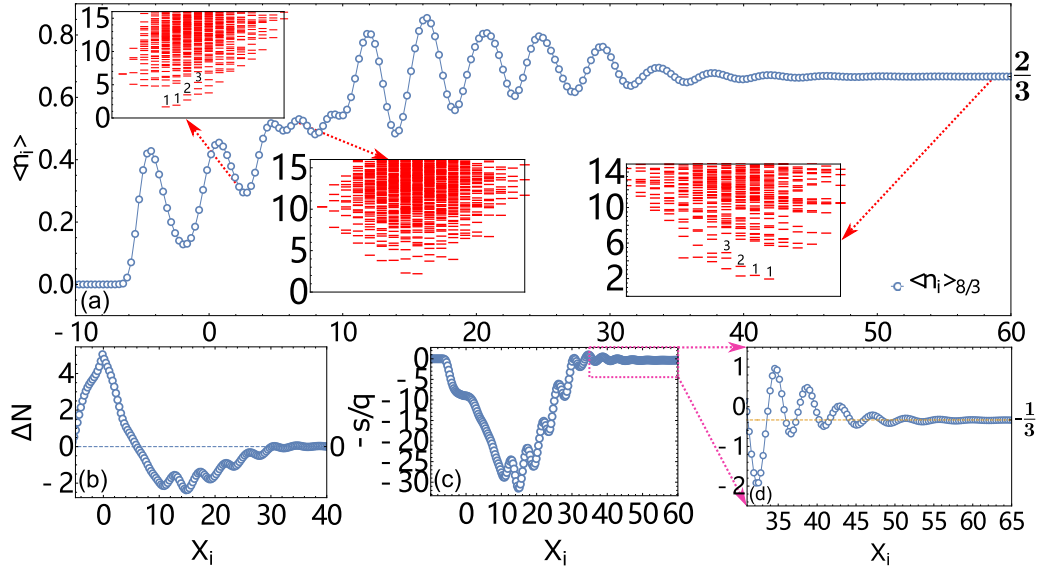
FIG. 12. *The $\nu = 2|\nu = 8/3$ interface:* (a) The density profile of the $\nu = 2|\nu = 8/3$ interface. The left half ($X_j < 0$) is the $\nu = 2$ ($\nu = 0$ in the SLL) state and the right ($X_j > 0$) is the $\nu = 8/3$ ($\nu = 2/3$ in the SLL) state. The insets show the ES in different positions. (b) The density integral of this interface. (c) The guiding-center spin extracted from the dipole moment. (d) A zoomed portion of (c). We can clearly see that $-s/q$ converges perfectly to $-1/3$ as the theoretical prediction. Here, we choose Coulomb interaction and the circumference $L_y = 21$.

A. Laughlin 1/3 state

The Laughlin 1/3 state is the simplest FQH state, and its topological characters have been extensively studied both numerically and theoretically. Here we use it as a benchmark. The Laughlin 1/3 state is an Abelian state with three kinds of quasiparticle, 0, $+|e|/3$, $-|e|/3$, and all of them have quantum dimension $d_a = 1$, thus the total quantum dimension is $\mathcal{D} = \sqrt{3}$ [76,86–88], so the TEE should be $\gamma_a = \ln\sqrt{3} \approx 0.549$. The EEs S_E of the Laughlin 1/3 state obtained using iDMRG have been shown in Fig. 3(a). Clearly, the EE satisfies the area law: $S_E \approx 0.157 L_y - \gamma$. In the lower panel of Fig. 3(a), the TEE γ converges to $\ln\sqrt{3} \approx 0.549$ as L_y increases.

The guiding-center spin of the Laughlin $1/q$ state is $s = \frac{1-q}{2}$ [81] (or see Appendix B), so the theoretical value of the Laughlin 1/3 state is $s = -1$ and topological spin is $h = \frac{1}{3}$ [81]. The numerical results of momentum polarization have been shown in Fig. 3(b), and they are in perfect agreement with the theoretical prediction as L_y increases. Finally, the edge theory of the Laughlin 1/3 state is described by a chiral free boson with central charge $c = 1$. In Fig. 3(b), the obtained c in momentum polarization perfectly converges to 1. Meanwhile, the ESs of the Laughlin 1/3 state have been shown in Fig. 4(a), which demonstrates explicitly that the chirality and the degeneracy of low-energy excitation are $1, 1, 2, 3, 5, \ldots$, which is consistent with theoretical prediction of the chiral free boson and with other numerical results [3,4,72,76,89,90].

B. The 2/3 state

Now we consider the $\nu = 2/3$ state, and we make a comparison with the 1/3 state. The topological characters are shown in Fig. 5. The lower panel shows that the TEE of the 2/3 state converges to $\ln\sqrt{3}$, similar to the Laughlin 1/3 state.

This value of the TEE shows the Abelian nature of the 2/3 state. Meanwhile, the ES of the 2/3 state in Fig. 4(b) also exhibits chirality and degeneracy, but its direction of motion is opposite to that of the Laughlin 1/3 state, which is shown in Fig. 4(a). This supports the idea that the $\nu = 2/3$ state is a hole-type Laughlin 1/3 state [84,85,91]:

$$S = \int dx\, dt\, \frac{1}{4\pi} \partial_x \phi_1 (\partial_t \phi_1 - v_1 \partial_x \phi_1)$$
$$- \frac{3}{4\pi} \partial_x \phi_3 (\partial_t \phi_3 + v_3 \partial_x \phi_3), \tag{36}$$

where ϕ_1 is the edge mode of the $\nu = 1$ component, and ϕ_3 is the edge mode of the Laughlin $\nu = 1/3$ component.

In addition, the momentum polarization is shown in Fig. 5; the topological spin of the 2/3 state is $h = 1/3$, but the guiding-center spin takes the opposite value $s \approx 1$, which is opposite to that of the 1/3 state, which is consistent with theoretical prediction (see Appendix B). From this, we also state that the topological shift is $\mathcal{S} = 0$ for the 2/3 state, pointing to the Abelian Laughlin state.

The numerically obtained chiral central charge perfectly converges to 0 as L_y increases. The result $c \approx 0$ supports two counterpropagating $\nu = 1$ and $1/3$ edge modes. This is also consistent with the exact diagonalization study on the torus geometry [81].

C. The $2 + 2/3$ state

We consider the $\nu = 8/3$ state in SLL. First, the ES is shown in the inset of Fig. 6(a), which shows the same ES as the ES of the 2/3 state. The typical $1, 1, 2, 3, 5, \ldots$ counting matches the prediction of a free chiral boson. In addition, the EE S_E scales as the area law in Fig. 6(a); the fitting result is $S_E \approx -0.3919 + 0.1813 L_y$. The extracted TEE is $\gamma \approx 0.3919$, which is nearly a 29% error from the theoretical
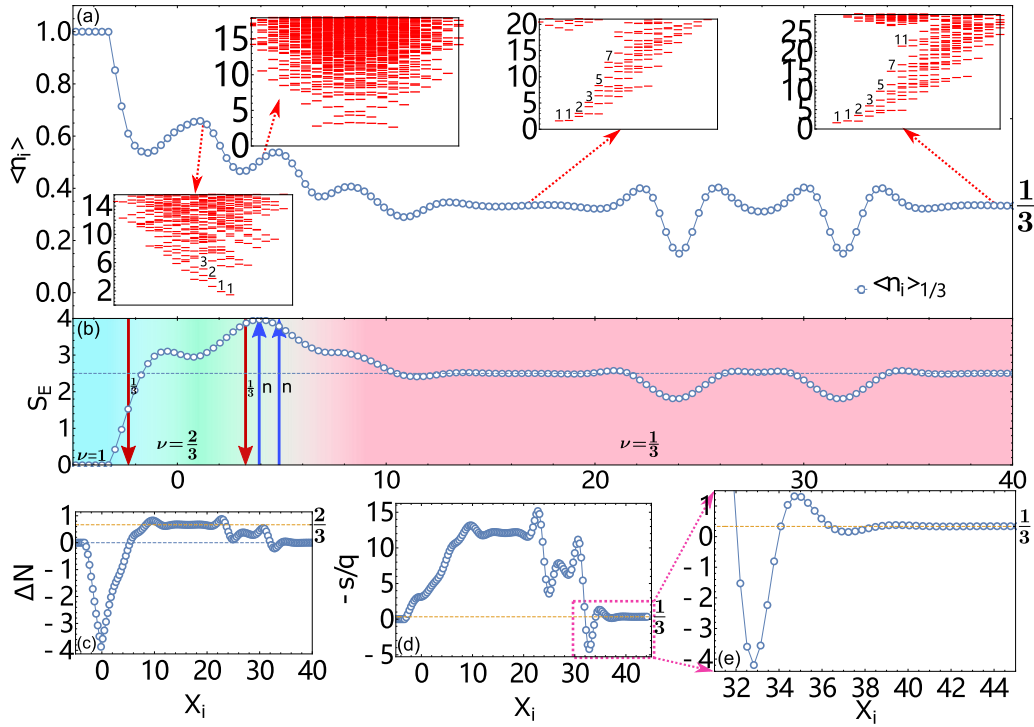
FIG. 13. *The $\nu = 1 | \nu = 1/3$ interface:* (a) The density profile of the $\nu = 1 | \nu = 1/3$ interface. The left half ($X_j < 0$) is the $\nu = 1$ state and the right ($X_j > 0$) is the $\nu = 1/3$ state. The insets show the ES in different positions. The ESs in region $X_i > 0\ell$ and $X_i > 10\ell$ have opposite chirality, which means a small region of 2/3 has emerged. The ES in the upper left corner ($X_i \approx 4\ell$) have particle-hole symmetry, which is evidence of the existence of the interface between the 1/3 and 2/3 states. (b) The EE of this interface, and the background is the schematic diagram of this interface; the red and blue arrows represent the 1/3 chiral boson and neutral mode, respectively. (c) The density integral of this interface. (d) The guiding-center spin extracted from the dipole moment. (e) A zoomed portion of (d). We can clearly see that $-s/q$ converges perfectly to 1/3 as the theoretical prediction. Here, we choose Haldane pseudopotential $v_1 = 1.0$ and the circumference $L_y = 20$.

prediction of the 2/3 state ($\ln \sqrt{3} \approx 0.5493$); the big error comes from the finite-size effect of L_y. The Coulomb interaction at SLL decays much slower than the lowest Landau level (LLL), resulting in a rapid increase of the bond dimension of MPO (~ 1000–2000), so it is difficult to get convergence in large L_y. On the other hand, the momentum polarization in Figs. 6(c) and 6(d) tells us that the 8/3 state contains only one kind of topological spin, $h_a = 1/3$, consistent with the Abelian 2/3 state. Moreover, the extracted guiding-center spin s and central charge c are shown in Figs. 6(c) and 6(d); they all oscillate and converge slowly to the theoretical value of the $\nu = 2/3$ state ($s = 1$ and $c = 0$) as L_y increases [92]. Combining the above results, we can conclude that the 8/3 state is Abelian, which is topologically equivalent to the 2/3 state in LLL.

IV. TOPOLOGICAL PROPERTIES ON THE HARDWALL EDGE

Apart from the topological order in bulk, we will investigate the edge of the 1/3, 2/3, 8/3 states in this section. Here, when we refer to the edge, it is equivalent to the "hardwall$|\nu$" interface as shown in Fig. 2 (top).

A. Density profile

The expectation of the particle number operator $\langle \hat{n}_i \rangle = \langle \hat{c}_i^\dagger \hat{c}_i \rangle$ is the most direct representation of the edge. We

plot the density profile of the edge [or the "hardwall" interface; see Fig. 2 (top)] of the $\nu = 1/3$ and 2/3 states in Fig. 7(a). The edge of the 1/3 state exhibits oscillating behavior, similar to Ref. [60], and the density profile can be well fitted by $f_\nu(x) = C_\nu \exp(-x/\xi_\nu) \cos(k_\nu x + \theta_\nu) + \nu$, where $k_{1/3} \approx 1.546\ell^{-1}$ and $\xi_{1/3} \approx 1.573\ell$. The wave number $k_{1/3} \approx 1.546\ell^{-1}$ is close to the bulk magnetoroton minimum, in agreement with the result in Refs. [60,93,94]. The density profile of the 2/3 state has a $\nu = 1$ integer region at the outmost. After an intermediate region, a typical oscillating behavior can be found ($X_j > 14\ell$) and the same fitting result as that of the 1/3 state ($k_{2/3} \approx 1.549\ell^{-1}$ and $\xi_{2/3} \approx 1.552\ell$). The results of the 8/3 state are shown in Fig. 8. There is also an outmost $\nu = 1$ integer region, where the typical oscillating behavior can be found in $X_j > 34\ell$ and the fitting results are $k_{8/3} \approx 1.517\ell^{-1}$ and $\xi_{8/3} \approx 5.482\ell$. The 2/3 and 8/3 edge profile is consistent with the theoretical prediction, which includes an outmost $\nu = 1$ edge and an inner $\nu = 1/3$ edge.

B. Dipole moment and guiding-center spin

The oscillating density induces a dipole moment on the edge. Before calculating the dipole moment, we should check the charge neutral conditions where the density integral $\Delta N(x) = \sum_i^x (\langle \hat{n}_i \rangle - \nu)$ should converge to 0 [47]. This condition ensures that the dipole moment does not depend on the choice of origin. In Figs. 7(b) and 8(b), we can see that
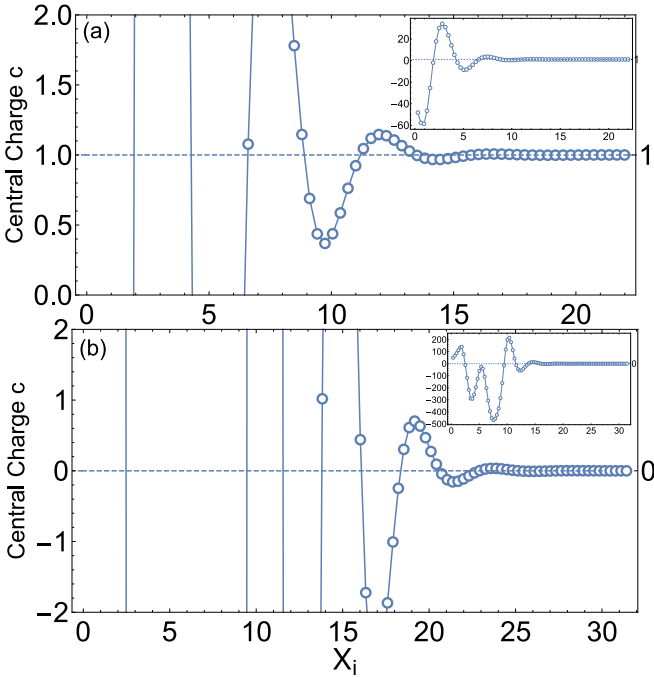
FIG. 14. *The central charge c of the $\nu = 1/3, 2/3$ state:* The extracted central charge c of (a) the Laughlin $\nu = 1/3$ state and (b) the $\nu = 2/3$ state from the density profile. The insets show the complete data range. The results are calculated by Eq. (C1); the density profile are the same data as in Fig. 7, and the guiding-center spin in Eq. (C1) is chosen to be $s_{1/3} = -1, s_{2/3} = 1$. The extracted central charges of $\nu = 1/3, 2/3$ states are $c = 0.999\,931, 0.000\,066$, respectively.

$\Delta N(x)$ converges to 0 in bulk. The dipole moment in an inhomogeneous external electric field will feel an electric force, and this force can be balanced by the viscous force. Thus the relation between Hall viscosity and dipole moment is $\eta_H^g = -\frac{\hbar}{4\pi\ell^2}\frac{s}{q} = \frac{2\pi|e|B}{L_y^2}\sum_i(\langle n_i\rangle - \nu)\times i$ [47,83], where we can extract the topological quantity guiding-center spin s via

$$-\frac{s}{q} = \frac{8\pi^2}{L_y^2}\sum_i(\langle n_i\rangle - \nu)\times i. \qquad (37)$$

We have shown the results of the Laughlin $1/3$ state in Fig. 7(c). The quantity $-s/q$ converges to $1/3$ in the bulk, and the extracted guiding-center spin is $s \approx -1$. The results of the $2/3$ and $8/3$ states are shown in Figs. 7(d) and Figs. 8(c) and 8(d), and the extracted guiding-center spin is $s_{2/3} \approx s_{8/3} \approx 1$. Both results are consistent with theoretical predictions (see Appendix B).

In particular, in Figs. 7(a) and 7(b) we can see a quasiparticle ($-|e|/3$) and a quasihole ($+|e|/3$) at $X_i \approx 14\ell$ and $X_i \approx 6.5\ell$, respectively. The same behavior can also be found in Fig. 8(b); the coordinates of the quasiparticle and quasihole are $X_i \approx 33\ell$ and $X_i \approx 14\ell$, respectively. This pair cancels out part of the dipole moment of the outermost integer region, leaving a quantized guiding-center spin.

V. TOPOLOGICAL PROPERTIES ON THE INTERFACE

The interface between different quantum Hall states is a useful geometry to study the edge physics, which can be realized in experiments. In particular, recent measurements on the interface between $\nu = 1$ and $2/3$ states demonstrate the counterpropagating chiral channels and upstream neutral edge mode [11–13]. Motivated by this experimental progress, in this section we study the interface between integer quantum Hall states and FQH states. The numerical details of constructing an interface in DMRG is the "cut-and-glue" scheme, which has been shown in Sec. II E.

A. The $\nu = 1 | \nu = 2/3$ interface

Let us recall that, in Sec. III B, the $\nu = 2/3$ state supports two counterpropagating chiral channels: a downstream $\nu = 1$ electron channel and an upstream $\nu = 1/3$ channel. On the interface between $\nu = 1$ and $2/3$ there is expected to be only one $1/3$ edge mode, since the integer edge mode of the $2/3$ state is gapped out by the $\nu = 1$ state. The single $1/3$ edge mode is expected to exhibit a $1/3$ two-terminal conductance, which has been seen in experiment [13]. Similarly, for a $\nu = 3 | \nu = 8/3$ interface, the two integer edge modes in the lower Landau level gap out each other, equivalent to a $\nu = 1 | \nu = 2/3$ interface.

The blue line in Fig. 9(a) is the density $\langle \hat{n}_i \rangle_{2/3}$ of this interface, the left half ($X_j < 0$) is the $\nu = 1$ state, and the right ($X_j > 0$) is the $\nu = 2/3$ state. We have found two interesting points from the density profile. First, there is no charge "leaking" from $\nu = 1$ to $2/3$, reflecting the incompressible nature of the $\nu = 2/3$ state. Second, we compare the density profile with the hole-Laughlin state $1 - \langle \hat{n}_i \rangle_{1/3}$, where $\langle \hat{n}_i \rangle_{1/3}$ is the density of the Laughlin $1/3$ state as shown in Fig. 7(a). It is found that the density profile around the $\nu = 1 | \nu = 1/3$ interface perfectly matches the hole-Laughlin state. This strongly indicates that the $\nu = 1 | \nu = 2/3$ interface forms a hole-type Laughlin $\nu = 1/3$ state.

Similar to Sec. IV B, the balance condition on the interface requires us to form a quantized electric dipole moment [83],

$$-\left(\frac{s^R}{q^R} - \frac{s^L}{q^L}\right) = \frac{8\pi^2}{L_y^2}\sum_i(\langle n_i\rangle - \nu_i)\times i, \qquad (38)$$

where $\nu_i = \theta(i)\times 1 + \theta(-i)\times 2/3$ is the filling of each half and $\theta(x)$ is the step function. In the left region $s^L = 0$ for the $\nu = 1$ state, and in the right region $s^R/q^R = 1/3$ for the $\nu = 2/3$ state (as shown in Sec. III B), and we expect $-1/3$ in Eq. (38) on the $\nu = 1 | \nu = 2/3$ interface. In Fig. 9(b), we have shown the numerical result of the dipole moment where the results converge to $-1/3$ perfectly as X_j increases.

Now we consider the similar $\nu = 3 | \nu = 3/8$ interface or the $\nu = 1 | \nu = 2/3$ interface in SLL; the results are shown in Fig. 10. In Fig. 10(a), we have shown the density of the $\nu = 3 | \nu = 2/3$ interface; the insets are ESs at different positions. In Fig. 10(b), the density integral converges to 0, indicating the neutral condition. Using Eq. (38) and choosing $\nu_{i<0} = 1, \nu_{i>0} = 2/3$, we have shown the results in Figs. 10(c) and 10(d). The result converges to $-1/3$ perfectly as X_j increases, which is consistent with the result of the $\nu = 1 | \nu = 2/3$ interface in the LLL. This result shows that the $\nu = 8/3$ state has the same guiding-center spin as the $\nu = 2/3$ state. It can be seen as evidence that the $\nu = 8/3$ and $2/3$ states have the same topological order.
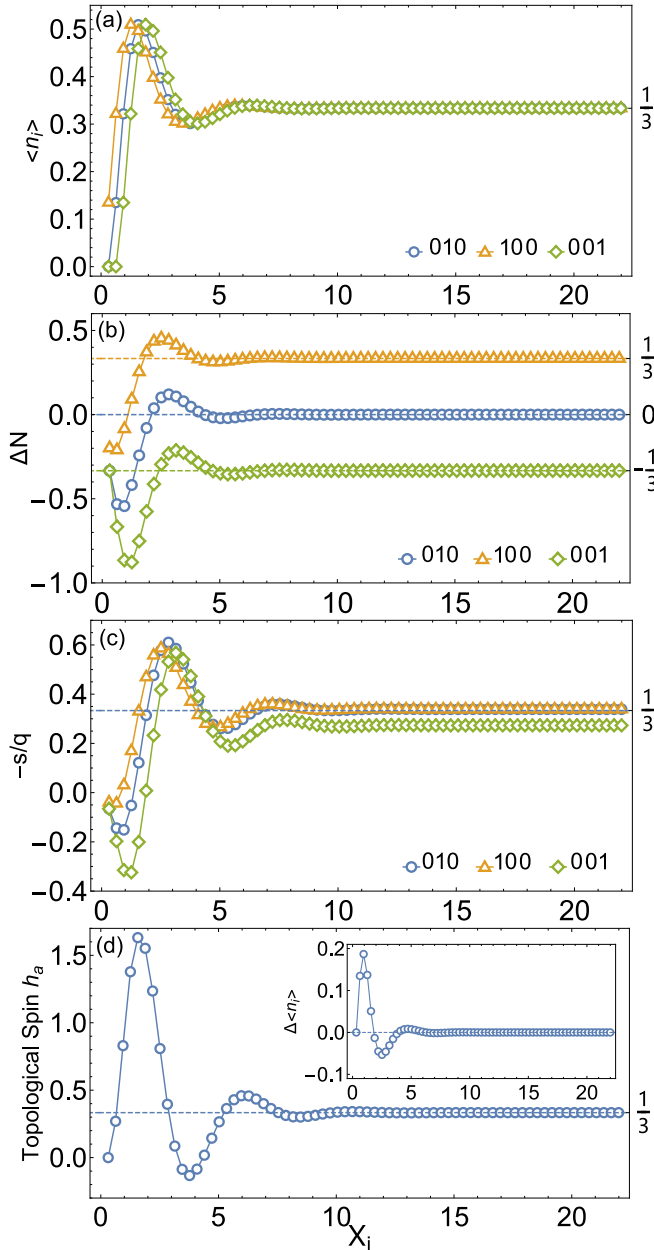
FIG. 16. *The "hardwall edge" of different topological sectors of the $\nu = 2/3$ state:* The topological spin extracted from the density profile; the result is $h_a \approx 0.333333$. The insets show the complete data range. Here, we choose the Haldane pseudopotential $v_1 = 1.0$ and the circumference of cylinder $L_y = 20\ell$.

FIG. 15. *The "hardwall edge" of different topological sectors of the Laughlin $\nu = 1/3$ state:* (a) The density profile $\langle \hat{n}_i \rangle$, (b) density integral ΔN, and (c) extracted $-s/q$ of different topological sectors of the Laughlin $\nu = 1/3$ state. (d) The topological spin of the 001 topological sector; the result is $h_a \approx 0.333332$. And the inset is the density difference $\Delta \langle \hat{n}_i \rangle = \langle \hat{n}_i \rangle_0 - \langle \hat{n}_i \rangle_a$ between different topological sectors. Here, we choose the Haldane pseudopotential $v_1 = 1.0$ and the circumference of cylinder $L_y = 20\ell$.

B. The $\nu = 0 | \nu = 2/3$ interface

We concentrate now on the interface between $\nu = 0$ and $2/3$, which is equivalent to the $\nu = 2 | \nu = 8/3$ interface. We stress that the difference between the $\nu = 0 | \nu = 2/3$ interface and the hardwall edge of $\nu = 2/3$ is as follows (see Sec. III B): the edge can be seen as a special interface with an infinite confining potential; under this potential, the electrons never cross the interface to the $\nu = 0$ region, and as a result an out-
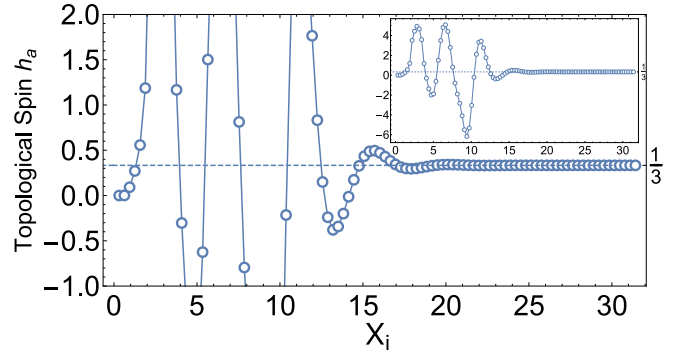
most $\nu = 1$ region is formed [see Fig. 7(a)]. Here, we choose the confining potential to be 0, therefore electrons cross the interface to the $\nu = 0$ region, and the original $\nu = 1$ region collapses, thus the edge reconstruction occurs. The former study [14] suggested that a $\nu = 1/3$ stripe will appear on the outmost region. As a result, two new counterpropagating $\nu = 1/3$ edge modes could be added to the outside of the original (in order from edge to bulk, $1/3, -1/3, 1, -1/3$) [10,38]. The former study proposed that the inner three edge modes should renormalize to a single $1/3$ charge mode and two opposite neutral modes.

In Fig. 11(a), the blue line is the density profile of the $\nu = 0 | \nu = 2/3$ interface, where the left half ($X_i < 0$) is vacuum $\nu = 0$ and the right ($X_i > 0$) is $\nu = 2/3$. We identify that the density in the $X_i < 0$ region forms a typical Laughlin $\nu = 1/3$ edge by comparing the density profile with that of the Laughlin $1/3$ state (the yellow line) [same data from Fig. 7(a)]. The inset at the bottom left of Fig. 11(a) is the entanglement spectrum at $X_i \approx 0.47\ell$, which shows the same chirality and counting as the Laughlin $\nu = 1/3$ state. Combining these two pieces of evidence, we can conclude that there is a $1/3$ edge mode at the outmost region ($-3\ell < X_i < 0$). Moving to $X_i \approx 4.39\ell$, the entanglement spectrum shown in the upper left corner of Fig. 11(a) exhibits particle-hole symmetry, signaling a crossover regime. Moreover, the entanglement spectrum on the right side of this point shows the same chirality as the $\nu = 2/3$ state. Based on these observations, we speculate that at around $X_i \approx 4.39\ell$ and $\langle \hat{n}_i \rangle \approx 0.5$ a $\nu = 1/3 | \nu = 2/3$ interface emerges. This is partially consistent with the prediction in Ref. [38] and experimental observation [10].

Now, we focus on the dipole moment of the $\nu = 0 | \nu = 2/3$ interface. The density integral $\Delta N(x) = \sum_i^x (\langle \hat{n}_i \rangle - \nu)$ is shown in Fig. 11(c), and we obtain $\Delta N(X_i) = 0$ for large X_i. We further calculate the dipole moment of this interface by Eq. (38). In Figs. 11(d) and 11(e), we have shown the numerical result of Eq. (38), where $-s^{\nu=2/3}/q$ converges to -0.3387 as X_j increases, and we extracted $s^{\nu=2/3} \approx 1.0162$. Thus, the dipole moment on the $\nu = 0 | \nu = 2/3$ interface is the same as the $\nu = 2/3$ edge, because both $\nu = 0$ and vacuum have the same guiding-center spin $s^{\nu=1} = 0$.
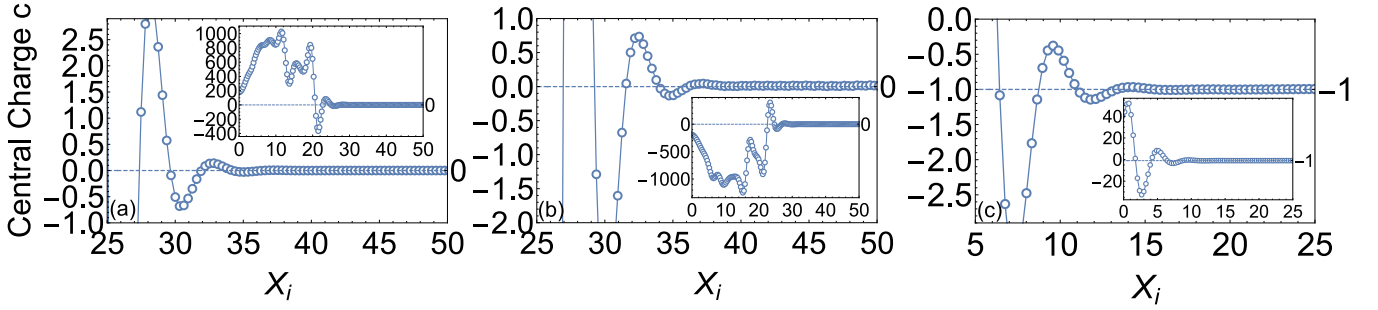
FIG. 17. *The central charge c of the interface:* The central charge of (a) $\nu = 1 | \nu = 1/3$ interface, (b) $\nu = 0 | \nu = 2/3$ interface, and (c) $\nu = 1 | \nu = 2/3$ interface. The results are $c \approx 0.000031$, $c \approx 0.013280$ and $c \approx -0.996121$ respectively.

Finally, we consider the $\nu = 2 | \nu = 8/3$ interface, where the integer parts gap each other out, leaving the $\nu = 0 | \nu = 2/3$ in the SLL. Comparing Figs. 11 and 12, we can see that the $\nu = 2 | \nu = 8/3$ interface is similar to the $\nu = 0 | \nu = 2/3$ interface, except for the different penetration depths (depending on the nonuniversal correlation length). One can see that there is also a small region of the $2 + 1/3$ Laughlin state between $\nu = 2$ and $8/3$, i.e., edge reconstruction occurs.

C. The $\nu = 1 | \nu = 1/3$ interface

At the end of this section we consider the $\nu = 1 | \nu = 1/3$ interface, which is also studied in Refs. [95,96]. The $\nu = 1 | \nu = 1/3$ interface is the particle-hole conjugation of the $\nu = 0 | \nu = 2/3$ interface. Meanwhile, in Sec. V B we find the edge reconstruction in the $\nu = 0 | \nu = 2/3$ interface, resulting in a small $\nu = 1/3$ region between $\nu = 0$ and $2/3$, thus we look forward to discovering a small $\nu = 2/3$ region on the $\nu = 1 | \nu = 1/3$ interface. Fortunately, in the insets of Fig. 13(a) we see that the ES around $X_i \approx 1.5\ell$ exhibits an achiral property, which indicates that a small $\nu = 2/3$ region

has emerged. Following the discussion in Sec. V B, we can see that the outmost edge mode comes from the $\nu = 1 | \nu = 2/3$ interface, i.e., a single $1/3$ charge mode [Fig. 13(b)]. As for the inside, a $1/3$ charge mode and two opposite neutral modes [Fig. 13(b)] come from the $\nu = 2/3 | \nu = 1/3$ interface. In Figs. 13(c) and 13(d), the extracted guiding-center spin is $\Delta s = s^{\nu=1/3} - s^{\nu=1} = -1$. Once again, this supports the idea that the dipole moment is a quantized quantity on the interface that is protected by intrinsic topology.

VI. CONCLUSION

In this paper, we investigate the topological properties of $\nu = 2/3$ and $8/3$ states, including the bulk and edge physics. On the one hand, via the entanglement spectra and momentum polarization calculations, we identify that both $2/3$, $8/3$ states are Abelian-type, and they share the same topology as the hole-conjugated Laughlin $1/3$ state. On the other hand, we illustrate the interface made of the $\nu = 2/3$ ($8/3$) states and $\nu = 0$ (2). Crucially, our method is able to demonstrate edge reconstruction directly, i.e., it shows that the interface
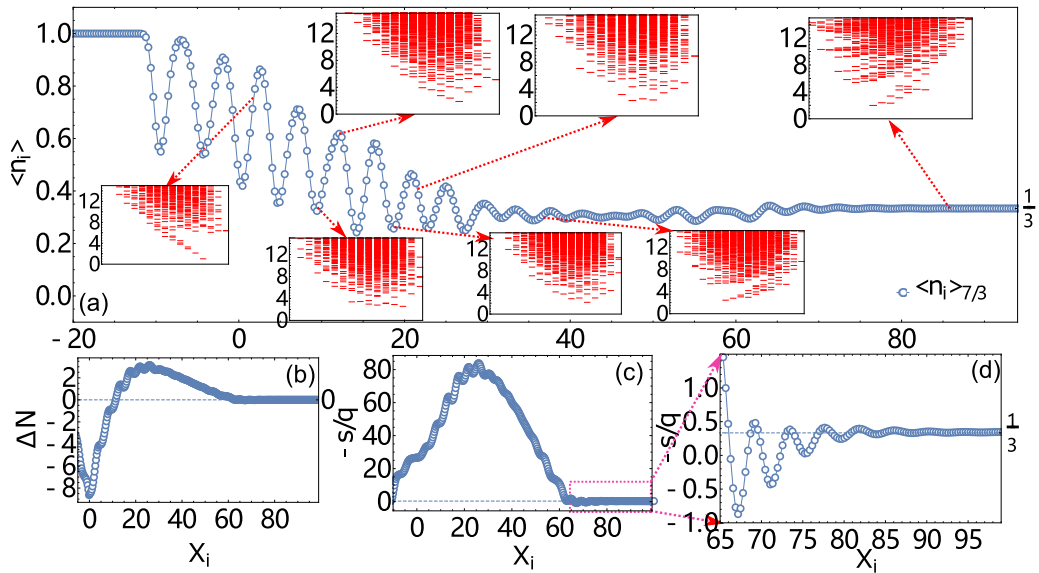

FIG. 18. *The $\nu = 2 | \nu = 7/3$ interface:* (a) The density profile of the $\nu = 2 | \nu = 7/3$ interface. The left half ($X_j < 0$) is the $\nu = 2$ ($\nu = 0$ in the SLL) state, and the right ($X_j > 0$) is $\nu = 7/3$ ($\nu = 1/3$ in the SLL) state. The insets show the ES in different positions. (b) The density integral of this interface. (c) The guiding-center spin extracted from the dipole moment. (d) A zoomed portion of (c); we can clearly see that $-s/q$ converge perfectly to $1/3$ as the theoretical prediction. Here, we choose Coulomb interaction and the circumference $L_y = 21$.
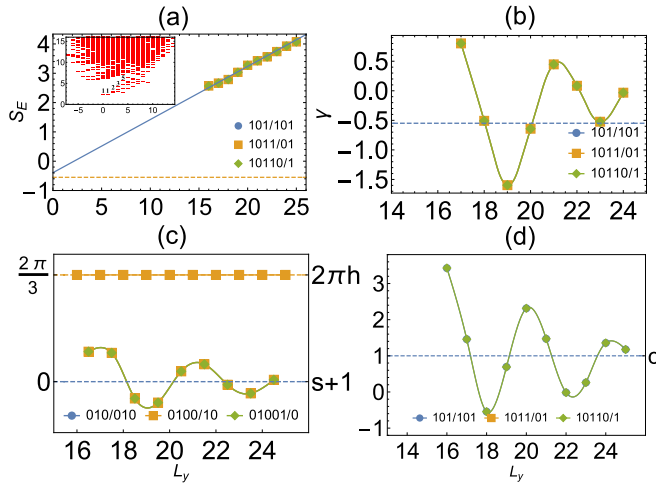
FIG. 19. *The topological characters of the $\nu = 7/3$ state for Coulomb interaction:* (a) The EE and (b) the extracted TEE of the $\nu = 7/3$ state; the yellow dashed line is $-\ln\sqrt{3}$. (c),(d) The momentum polarization of the $\nu = 7/3$ state in different L_y. Part (c) shows the extracted topological spin h_a and guiding-center spin s, while (d) is the central charge c.

$\nu = 0|\nu = 2/3$ contains a 1/3 edge mode and a group of edge modes inherited from the $\nu = 1/3|\nu = 2/3$ interface, which are spatially separated on the interface. Throughout this paper, we find that the dipole moment living on the interface is a quantized quantity (equivalent to guiding-center spin or topological shift) which is protected by nontrivial topology, even though charge density is nonuniversal depending on the interaction details. Lastly, in the case of a hardwall edge (a sharp confining potential), edge reconstruction does not occur, and the edge state forms a group with the outer $\nu = 1$ integer quantum Hall mode and an inner counterpropagating 1/3 mode.

These results open the door to looking at fractional states and the behavior of edge modes, especially in cases in which reconstruction at the edge takes place, leading to the formation of counterpropagating modes. For example, it was experimentally identified [9,10] and then theoretically proposed [38] that the reconstructed edge at the 2/3 state consists of an outermost 1/3 channel and the inner composite channels including neutral modes. Our current results indeed support the above picture (on the interface or smooth edge potentials), which has not been achieved by numerical simulations before. Thus, we believe that our work paves the way to a more complete understanding of fractional quantum Hall states, and it can be extended to more fillings without any barrier.

ACKNOWLEDGMENTS

APPENDIX A: DETAILS OF THE MANY-BODY HAMILTONIAN

In this Appendix, we will show more details about the derivation of the Hamiltonian and the Fourier transformation of the modified Coulomb interaction.

1. Hamiltonian

First, the Landau level wave function is

$$\psi_{n,j}(x, y) = \frac{e^{-i\frac{X_j}{\ell^2}y - \frac{(x-X_j)^2}{2\ell^2}}}{\sqrt{2^n n!\sqrt{\pi}\ell L_y}}H_n\left(\frac{x-X_j}{\ell}\right). \quad (A1)$$

If we project the electron-electron interaction into a single Landau level, the second quantization form of the Hamiltonian can be expressed by

$$H_I = \sum_{j_1,j_2,j_3,j_4}^{N_\phi} A^n_{j_1,j_2,j_3,j_4}a^\dagger_{n,j_1}a^\dagger_{n,j_2}a_{n,j_3}a_{n,j_4}, \quad (A2)$$

where the interaction matrix element is

$$A^n_{j_1,j_2,j_3,j_4} = \frac{1}{2}\int dr_1 \int dr_2 \psi^*_{N,j_1}(r_1)\psi^*_{N,j_2}(r_2)$$
$$V(r_1, r_2)\psi_{N,j_3}(r_2)\psi_{N,j_4}(r_1). \quad (A3)$$

The two-body interaction in real space satisfies $V(r + b\hat{e}_y) = V(r)$, which we can rewrite as

$$V(r) = \frac{1}{L_y}\int_{-\infty}^{\infty}dq_x \sum_{q_y} V(q)e^{iq \cdot r}, \quad (A4)$$

where $q_y = \frac{2\pi t}{L_y}$, $t \in \mathbb{Z}$ is the momentum along the y-direction, and

$$V(q) = \int_{-\infty}^{\infty}dx \int_0^{L_y} dy\, V(r)e^{iq \cdot r}. \quad (A5)$$

Now we can calculate $A^N_{j_1,j_2,j_3,j_4}$ by substituting Eq. (A4) into Eq. (A3):

$$A^N_{j_1,j_2,j_3,j_4} = \frac{1}{2L_y}\int_{-\infty}^{\infty}dq_x \sum_{q_y} V(q)I^N_{j_1,j_4}(q)I^N_{j_2,j_3}(-q), \quad (A6)$$

where $I^N_{s,s'}(q) = \int dr\,\psi^*_{N,s}\psi_{N,s'}e^{iq \cdot r}$ is a useful integral:

$$I^n_{s,s'}(q) = \frac{1}{2^n n!\sqrt{\pi}\ell}\int_{-\infty}^{\infty}dx\, e^{-\frac{1}{\ell^2}\left[x-\frac{1}{2}(2X_s - q_y\ell^2 + iq_x\ell^2)\right]^2}$$
$$\times H_n[(x-X_s)/\ell]H_n[(x-X_{s'})/\ell]$$
$$\times e^{\frac{1}{4\ell^2}(2X_s - q_y\ell^2 + iq_x\ell^2)^2 - \frac{X_s^2}{2\ell^2} - \frac{(X_s - q_y\ell^2)^2}{2\ell^2}}\delta_{t,s-s'}$$
$$= L_n\left(\frac{1}{2}q^2\ell^2\right)e^{-\frac{1}{4}q^2\ell^2 + iq_x X_s - \frac{iq_x q_y\ell^2}{2}}\delta_{t,s-s'}. \quad (A7)$$

We first integrate the variable y and then use a special function integral relation $\int_{-\infty}^{\infty}dx\, e^{-x^2}H_m(x+y)H_n(x+z) = 2^n\sqrt{\pi}m!z^{n-m}L_m^{n-m}(-2yz)\, m \leqslant n$.

Finally, we have

$$
\begin{aligned}
A^n_{j_1, j_2, j_3, j_4} &= \frac{1}{2b} \int_{-\infty}^{\infty} dq_x \sum_{q_y} V(q) I^n_{j_1, j_4}(\boldsymbol{q}) I^n_{j_2, j_3}(-\boldsymbol{q}) \\
&= \frac{1}{2L_y} \int_{-\infty}^{\infty} dq_x \sum_{q_y} V(q) \left[L_N \left(\frac{1}{2} q^2 \ell^2 \right) \right]^2 \\
&\quad \times e^{-\frac{1}{2} q^2 \ell^2 + i q_x (j_1 - j_3) \frac{2\pi \ell^2}{L_y}} \delta_{q_y, \frac{2\pi(j_1 - j_4)}{L_y}} \delta_{j_1 + j_2, j_3 + j_4}.
\end{aligned}
$$
(A8)

2. Fourier transformation of the modified Coulomb interaction

The modified Coulomb interaction in real space is $V(\boldsymbol{r}) = \frac{e^2}{\epsilon} \frac{e^{-r^2/\xi^2}}{r}$. Due to the periodicity along the y-direction, it can be written as

$$
V(\boldsymbol{r}) = \frac{e^2}{\epsilon} \sum_{t \in \mathbb{Z}} \frac{e^{-r^2/\xi^2}}{|\boldsymbol{r} + tb\hat{\boldsymbol{e}}_y|} = \frac{1}{b} \int_{-\infty}^{\infty} dq_x \sum_{q_y} V(\boldsymbol{q}), \quad (\text{A9})
$$

where $\boldsymbol{r} \cdot \hat{\boldsymbol{e}}_y \in [0, L_y]$ and $q_y = \frac{2\pi t}{L_y}, t \in \mathbb{Z}$. We have

$$
\begin{aligned}
V(\boldsymbol{q}) &= \frac{1}{2\pi} \frac{e^2}{\epsilon} \int_{-\infty}^{\infty} dx \int_{-\infty}^{\infty} dy \frac{e^{-r^2/\xi^2}}{r} e^{-i\boldsymbol{q}\cdot\boldsymbol{r}} \\
&= \frac{1}{2\pi} \frac{e^2}{\epsilon} \int_0^{\infty} dr \int_0^{2\pi} d\theta \frac{e^{-r^2/\xi^2}}{r} e^{-iqr\cos\theta} \\
&= \frac{e^2}{\epsilon} \int_0^{\infty} dr\, e^{-r^2/\xi^2} J_0(qr) \\
&= \frac{e^2}{\epsilon} \frac{\xi}{2} \sqrt{\pi} \exp \left(-\frac{q^2\xi^2}{8} \right) I_0 \left(\frac{q^2\xi^2}{8} \right),
\end{aligned}
$$
(A10)

where $\int_0^{\infty} dr\, e^{-r^2/\xi^2} J_0(r) = \frac{\xi}{2} \sqrt{\pi} \exp(-\xi^2/8) I_0(\xi^2/8)$ and $I_0(z) = \frac{1}{\pi} \int_0^{\pi} \exp(z\cos\theta)\cos(n\theta) d\theta$ is the *first modified Bessel function* $I_n(z) = \frac{1}{\pi} \int_0^{\pi} d\theta \exp(z\cos\theta)\cos(n\theta)$. If we choose $\xi \to \infty$, the modified Coulomb interaction with regulated length ξ will come back to the original Coulomb interaction,

$$
\lim_{\xi \to \infty} V(\boldsymbol{q}) = \frac{e^2}{\epsilon} \frac{1}{q}, \quad (\text{A11})
$$

where we have used the asymptotic approximation of the first kind of modified Bessel function (for large values of x),

$$
I_n(x) = \frac{e^x}{\sqrt{2\pi x}} \left[1 - \frac{4n^2 - 1}{8x} + O\left(\frac{1}{x^2} \right) \right]. \quad (\text{A12})
$$

3. Pseudopotential Hamiltonian

In general, the $V(\boldsymbol{q})$ in Eq. (A4) can be expanded with Laguerre polynomials,

$$
V(\boldsymbol{q}) = \sum_l v_l L_l(q^2), \quad (\text{A13})
$$

where $L_l(x)$ is a Laguerre polynomial and v_l are some tunable parameters.

Here, we will show that this potential is a short-range interaction, using Eq. (A4),

$$
\begin{aligned}
V(\boldsymbol{r}) &= \frac{1}{L_y} \int_{-\infty}^{\infty} dq_x \sum_{q_y} \sum_l v_l L_l(q^2) e^{i\boldsymbol{q}\cdot\boldsymbol{r}} \\
&= \sum_l v_l L_l(-\nabla_r^2) \int_{-\infty}^{\infty} dq_x \frac{1}{L_y} \sum_{q_y} e^{i\boldsymbol{q}\cdot\boldsymbol{r}} \\
&= \sum_l v_l L_l(-\nabla_r^2) \delta^2(\boldsymbol{r}).
\end{aligned}
$$
(A14)

This is the model Hamiltonian of the Laughlin $\nu = 1/q$ wave function $\Psi_q(\{\boldsymbol{r}_i\})$,

$$
\int \prod_i d^2\boldsymbol{r}_i \Psi_q^*(\{\boldsymbol{r}_i\}) \sum_{j,k} V(\boldsymbol{r}_j - \boldsymbol{r}_k) \Psi_q(\{\boldsymbol{r}_i\}) = 0 \quad (\text{A15})
$$

if we choose

$$
\begin{aligned}
v_l &= 1 \quad (l < q), \\
v_l &= 0 \quad (l \geqslant q).
\end{aligned}
\quad (\text{A16})
$$

Since Laguerre polynomials are complete, by selecting the appropriate v_l's we can construct some special potential $V(\boldsymbol{r})$, and v_l is called the Haldane pseudopotential in order l.

APPENDIX B: THE THEORETICAL PREDICTION OF TOPOLOGICAL SHIFT

The topological shift, first introduced by Wen and Zee [44], is a shift in the relation between N_e and N_ϕ,

$$
N_\phi = \nu^{-1} N_e - \mathcal{S}(1 - g), \quad (\text{B1})
$$

where g is the genus of the manifold. We can easily find the relations $N_\phi = \nu^{-1} N_e - \mathcal{S}$ for sphere geometry and $N_\phi = \nu^{-1} N_e$ for torus geometry. In Ref. [44], the topological shift can be determined by the K matrix,

$$
\mathcal{S} = \frac{2}{\nu} \boldsymbol{q}^T K^{-1} \boldsymbol{s}, \quad (\text{B2})
$$

where $\boldsymbol{q}$ and $\boldsymbol{s}$ are charge and spin vectors. For the Laughlin $\nu = 1/q$ state in the LLL, where $K = q$, $\boldsymbol{q} = 1$, and $\boldsymbol{s} = q/2$, we have $\mathcal{S} = q$. As for the hole-type Laughlin state in filling $\nu = 1 - 1/q$ in the LLL, $K, \boldsymbol{q}, \boldsymbol{s}$ are

$$
K = \begin{pmatrix} 1 & 1 \\ 1 & 1 - q \end{pmatrix} \quad \boldsymbol{q} = \begin{pmatrix} 1 \\ 0 \end{pmatrix} \quad \boldsymbol{s} = \frac{1}{2} \begin{pmatrix} 1 \\ 1 - q \end{pmatrix}, \quad (\text{B3})
$$

thus we have $\mathcal{S} = 0$. Using the relations in Eq. (31), we have $s^{\frac{1}{q}} = \frac{1-q}{2}$ and $s^{1-\frac{1}{q}} = \frac{q-1}{2} = -s^{\frac{1}{q}}$. Now we consider the results in the higher Landau level. The K matrix and charge vector $\boldsymbol{q}$ do not change, but the components of spin vector s_I should change as the Landau level index n ($n = 0, 1, 2, \ldots$),

$$
s_I \to s_I + n. \quad (\text{B4})
$$

Now we have the final results,

$$
\begin{aligned}
\mathcal{S}^{n+\frac{1}{q}} &= q + 2n, \quad s^{n+\frac{1}{q}} = \frac{1-q}{2}, \\
\mathcal{S}^{n+1-\frac{1}{q}} &= 2n, \quad s^{n+1-\frac{1}{q}} = \frac{q-1}{2}.
\end{aligned}
\quad (\text{B5})
$$

We can clearly see that the guiding-center spin of the Laughlin $\nu = n + \frac{1}{q}$ state and its particle-hole conjugated $\nu = n + 1 - \frac{1}{q}$ state take opposite values. When we choose $q = 3$, we have the theoretical predictions of the Laughlin $\nu = n + \frac{1}{3}$ and $\nu = n + \frac{2}{3}$ states,

$$\mathcal{S}^{n+\frac{1}{3}} = 3 + 2n, \quad s^{n+\frac{1}{3}} = -1,$$
$$\mathcal{S}^{n+\frac{2}{3}} = 2n, \quad s^{n+\frac{2}{3}} = 1. \tag{B6}$$

The topological shift will change as the Landau level index changes, but the difference $2n$ is exactly the difference of Landau level degeneracy on the sphere. Please note that the degeneracy of the nth Landau level on the sphere is $N_o = 2s_0 + 1 + 2n$ ($n = 0, 1, 2, \dots$) [49,97], where s_0 is the number of monopoles on the center of the sphere, and $N_\phi = 2s_0$ is the number of magnetic Dirac flux quanta through the surface of the sphere. In addition, the guiding-center spin does not change as the Landau level index changes, thus it can be used to characterize the topological order of the FQH state in the higher Landau level.

APPENDIX C: CENTRAL CHARGE AND TOPOLOGICAL SPIN IN THE DIPOLE MOMENT

In this Appendix, we will show more numerical details about the $O(L_y^{-2})$ term in Eq. (34).

We first consider the dipole moment of the "hardwall edge" of the vacuum sector ($h_a = 0$). The central charge c can be extracted by

$$c = 24\left(\sum_i(\langle \hat{n}_i\rangle - \nu)i + \frac{L_y^2}{8\pi^2}\frac{s}{q}\right) + \nu. \tag{C1}$$

Using this equation, we have plotted the results of the $\nu = 1/3, 2/3$ states in Fig. 14. The extracted central charges of the $\nu = 1/3, 2/3$ states are $c = 0.999\,931, 0.000\,066$, respectively, in excellent agreement with theoretical predictions.

So far, we have only cut the infinite cylinder into a vacuum sector. Now we focus on the quasiparticle sector, which includes nonzero topological spin. Motivated by this intuition, we need to cut the infinite cylinder into different topological sectors. For example, the Laughlin $\nu = 1/3$ state has three distinct topological sectors that can be constructed by cutting the infinite cylinder $\cdots 010010\cdots$ into $|010010\cdots, |10010\cdots$, and $|0010\cdots$, respectively, where "|" denotes the "hardwall edge" and "$\cdots$" denotes the semi-infinite cylinder. We denote the three sectors as 010, 100, and 001. We use the same method as in Sec. II E to optimize the MPS, and the results are shown in Fig. 15(a). From the density integral in Fig. 15(b), we can clearly see that there is a quasiparticle of the 100 (001) sector with charge $Q_a = e/3$ ($-e/3$). As shown in Fig. 15(c), we have found that the dipole moment of the 001 sector is smaller than 010 (vacuum sector). The difference comes from the nonzero topological spin h_a. Using Eq. (34), the topological spin can be extracted from the density difference between

the vacuum ($\langle \hat{n}_i\rangle_0$) and the quasiparticle ($\langle \hat{n}_i\rangle_a$) sector by

$$h_a = \sum_i(\langle \hat{n}_i\rangle_0 - \langle \hat{n}_i\rangle_a)i. \tag{C2}$$

Using this relation, we have shown the results of $\nu = 1/3, 2/3$ in Figs. 15(d) and 16, respectively. The extracted topological spin is $h_a \approx 0.333\,332$ and $h_a \approx 0.333\,333$, and both results are consistent with theoretical predictions.

Finally, we consider the interface version of Eq. (C1). Using Eqs. (34) and (38), we have

$$c = 24\left(\sum_i(\langle \hat{n}_i\rangle - \nu_i)i + \frac{L_y^2}{8\pi^2}\left(\frac{s^R}{q^R} - \frac{s^L}{q^L}\right)\right) + \nu^R - \nu^L, \tag{C3}$$

where c is the central charge of the interface CFT. In Fig. 17, we have plotted the central charge c of the $\nu = 1|\nu = 1/3$, $\nu = 0|\nu = 2/3$, and $\nu = 1|\nu = 2/3$ interfaces, and we have used the same data as in Figs. 9, 11, 13. (a) $\nu = 1|\nu = 1/3$ interface: Following the discussion in Sec. V C, this interface includes two 1/3 charged modes and two counterpropagating neutral modes; the total central charge is 0. In Fig. 17(a), the numerical result is $c \approx 0.000\,031$, consistent with the theoretical value 0. (b) $\nu = 0|\nu = 2/3$ interface: The $\nu = 0|\nu = 2/3$ interface is the same as the $\nu = 1|\nu = 1/3$ interface, but all of the chiral edge modes have the opposite direction, so the theoretical value of the central charge is also 0. In Fig. 17(b), the extracted central charge is $c \approx 0.013\,280$. (c) $\nu = 1|\nu = 2/3$ interface: First, the edge theory of the $\nu = 2/3$ state is an integer mode and a counterpropagating 1/3 chiral charged mode. When we put the $\nu = 2/3$ state together with the $\nu = 1$ state, we see that the integer charged mode of the $\nu = 2/3$ state has been gapped; only a single 1/3 chiral charged mode with opposite chirality (or the edge mode of the hole-type Laughlin $\nu = 1/3$ state) remains. So, the central charge of the $\nu = 1|\nu = 2/3$ interface is $c = -1$. In Fig. 17(c), we have shown the central charge, and the result is $c \approx -0.996\,121$. All three of the numerical results in Fig. 17 are consistent with theoretical predictions. We conclude, therefore, that Eq. (C3) can be used to calculate the central charge of the interface.

APPENDIX D: $\nu = 7/3$ STATE

In this Appendix, we will show the results of the $\nu = 7/3$ state for the sake of completeness. The topological characters of the $\nu = 7/3$ state are shown in Fig. 19. The results indicate that the $\nu = 7/3$ and Laughlin $\nu = 1/3$ states share the same topological order, which is consistent with the conclusion in Ref. [48].

According to previous conclusions, we expect that the phenomenon of edge reconstruction will also occur on the $\nu = 2|\nu = 7/3$ interface. Fortunately, in the insets of Fig. 18(a), we can see that the ESs show same behavior as in Fig. 13. First, the ES around $X_i \approx 1.5\ell$ exhibits an achiral property, which indicates that a small $\nu = 2/3$ region has emerged. And then, in the rightmost region, the ESs are just those in the bulk of the $\nu = 7/3$ state. Finally, we find that in the intermediate region, the ESs exhibit particle-hole symmetry. Combining the above results, as we predicted, it can be seen that the edge reconstruction phenomenon occurred in the $\nu = 2|\nu = 7/3$ interface.

[1] D. C. Tsui, H. L. Stormer, and A. C. Gossard, Phys. Rev. Lett. **48**, 1559 (1982).

[2] R. B. Laughlin, Phys. Rev. Lett. **50**, 1395 (1983).

[3] X.-G. Wen, Int. J. Mod. Phys. B **04**, 239 (1990).

[4] X.-G. Wen, Int. J. Mod. Phys. B **06**, 1711 (1992).

[5] C. L. Kane, M. P. A. Fisher, and J. Polchinski, Phys. Rev. Lett. **72**, 4129 (1994).

[6] C. de C. Chamon and X. G. Wen, Phys. Rev. B **49**, 8227 (1994).

[7] X. Wan, K. Yang, and E. H. Rezayi, Phys. Rev. Lett. **88**, 056802 (2002).

[8] A. H. MacDonald, S. Eric Yang, and M. D. Johnson, Aust. J. Phys. **46**, 345 (1993).

[9] A. Bid, N. Ofek, M. Heiblum, V. Umansky, and D. Mahalu, Phys. Rev. Lett. **103**, 236802 (2009).

[10] R. Sabo, I. Gurman, A. Rosenblatt, F. Lafont, D. Banitt, J. Park, M. Heiblum, Y. Gefen, V. Umansky, and D. Mahalu, Nat. Phys. **13**, 491 (2017).

[11] Y. Cohen, Y. Ronen, W. Yang, D. Banitt, J. Park, M. Heiblum, A. D. Mirlin, Y. Gefen, and V. Umansky, Nat. Commun. **10**, 1920 (2019).

[12] A. Grivnin, H. Inoue, Y. Ronen, Y. Baum, M. Heiblum, V. Umansky, and D. Mahalu, Phys. Rev. Lett. **113**, 266803 (2014).

[13] B. Dutta, W. Yang, R. A. Melcer, H. K. Kundu, M. Heiblum, V. Umansky, Y. Oreg, A. Stern, and D. Mross, Science **375**, 193 (2022).

[14] Y. Meir, Phys. Rev. Lett. **72**, 2624 (1994).

[15] C. L. Kane and M. P. A. Fisher, Phys. Rev. B **55**, 15832 (1997).

[16] T. Chakraborty and P. Pietiläinen, Phys. Rev. Lett. **83**, 5559 (1999).

[17] N. Shibata and K. Nomura, J. Phys. Soc. Jpn. **76**, 103711 (2007).

[18] M. R. Peterson, Y.-L. Wu, M. Cheng, M. Barkeshli, Z. Wang, and S. Das Sarma, Phys. Rev. B **92**, 035103 (2015).

[19] S. C. Davenport and S. H. Simon, Phys. Rev. B **85**, 245303 (2012).

[20] W. Pan, K. W. Baldwin, K. W. West, L. N. Pfeiffer, and D. C. Tsui, Phys. Rev. Lett. **108**, 216804 (2012).

[21] J. P. Eisenstein, H. L. Stormer, L. N. Pfeiffer, and K. W. West, Phys. Rev. B **41**, 7910 (1990).

[22] L. W. Engel, S. W. Hwang, T. Sajoto, D. C. Tsui, and M. Shayegan, Phys. Rev. B **45**, 3418 (1992).

[23] J. H. Smet, R. A. Deutschmann, W. Wegscheider, G. Abstreiter, and K. von Klitzing, Phys. Rev. Lett. **86**, 2412 (2001).

[24] N. Freytag, Y. Tokunaga, M. Horvatić, C. Berthier, M. Shayegan, and L. P. Lévy, Phys. Rev. Lett. **87**, 136801 (2001).

[25] F. Schulze-Wischeler, E. Mariani, F. Hohls, and R. J. Haug, Phys. Rev. Lett. **92**, 156401 (2004).

[26] V. S. Khrapai, A. A. Shashkin, M. G. Trokina, V. T. Dolgopolov, V. Pellegrini, F. Beltram, G. Biasiol, and L. Sorba, Phys. Rev. Lett. **99**, 086802 (2007).

[27] S. K. Srivastav, R. Kumar, C. Spånslätt, K. Watanabe, T. Taniguchi, A. D. Mirlin, Y. Gefen, and A. Das, Phys. Rev. Lett. **126**, 216803 (2021).

[28] R. A. Melcer, B. Dutta, C. Spånslätt, J. Park, A. D. Mirlin, and V. Umansky, Nat. Commun. **13**, 376 (2022).

[29] R. Kumar, S. K. Srivastav, C. Spånslätt, K. Watanabe, T. Taniguchi, Y. Gefen, A. D. Mirlin, and A. Das, Nat. Commun. **13**, 213 (2022).

[30] J. Park, A. D. Mirlin, B. Rosenow, and Y. Gefen, Phys. Rev. B **99**, 161302(R) (2019).

[31] C. Spånslätt, J. Park, Y. Gefen, and A. D. Mirlin, Phys. Rev. Lett. **123**, 137701 (2019).

[32] I. Protopopov, Y. Gefen, and A. Mirlin, Ann. Phys. **385**, 287 (2017).

[33] C. Nosiglia, J. Park, B. Rosenow, and Y. Gefen, Phys. Rev. B **98**, 115408 (2018).

[34] A. V. Shchepetilnikov, D. D. Frolov, Y. A. Nefyodov, I. V. Kukushkin, L. Tiemann, C. Reichl, W. Dietsche, and W. Wegscheider, Phys. Rev. B **96**, 161301(R) (2017).

[35] Y. Meir, Int. J. Mod. Phys. B **10**, 1425 (1996).

[36] Z.-X. Hu, H. Chen, K. Yang, E. H. Rezayi, and X. Wan, Phys. Rev. B **78**, 235315 (2008).

[37] Y.-H. Wu, G. J. Sreejith, and J. K. Jain, Phys. Rev. B **86**, 115127 (2012).

[38] J. Wang, Y. Meir, and Y. Gefen, Phys. Rev. Lett. **111**, 246803 (2013).

[39] H. Meier, Y. Gefen, and L. I. Glazman, Phys. Rev. B **90**, 081101(R) (2014).

[40] N. Read and E. Rezayi, Phys. Rev. B **59**, 8084 (1999).

[41] M. Barkeshli and X.-G. Wen, Phys. Rev. B **81**, 045323 (2010).

[42] A. Vaezi and M. Barkeshli, Phys. Rev. Lett. **113**, 236804 (2014).

[43] P. Bonderson and J. K. Slingerland, Phys. Rev. B **78**, 125323 (2008).

[44] X. G. Wen and A. Zee, Phys. Rev. Lett. **69**, 953 (1992).

[45] M. P. Zaletel, R. S. K. Mong, and F. Pollmann, Phys. Rev. Lett. **110**, 236801 (2013).

[46] H.-H. Tu, Y. Zhang, and X.-L. Qi, Phys. Rev. B **88**, 195412 (2013).

[47] Y. J. Park and F. D. M. Haldane, Phys. Rev. B **90**, 045123 (2014).

[48] M. P. Zaletel, R. S. K. Mong, F. Pollmann, and E. H. Rezayi, Phys. Rev. B **91**, 045115 (2015).

[49] F. D. M. Haldane, Phys. Rev. Lett. **51**, 605 (1983).

[50] B. A. Bernevig and N. Regnault, Phys. Rev. B **85**, 075128 (2012).

[51] F. D. M. Haldane, Phys. Rev. Lett. **55**, 2095 (1985).

[52] S. R. White, Phys. Rev. Lett. **69**, 2863 (1992).

[53] U. Schollwöck, Ann. Phys. **326**, 96 (2011), January 2011 Special Issue.

[54] A. E. Feiguin, E. Rezayi, C. Nayak, and S. Das Sarma, Phys. Rev. Lett. **100**, 166803 (2008).

[55] J. Zhao, D. N. Sheng, and F. D. M. Haldane, Phys. Rev. B **83**, 195135 (2011).

[56] M. Fishman, S. R. White, and E. M. Stoudenmire, arXiv:2007.14822.

[57] B. A. Bernevig and F. D. M. Haldane, Phys. Rev. Lett. **100**, 246802 (2008).

[58] M. Yang and S. R. White, Phys. Rev. B **102**, 094315 (2020).

[59] S. R. White, Phys. Rev. B **72**, 180403(R) (2005).

[60] T. Ito and N. Shibata, Phys. Rev. B **103**, 115107 (2021).

[61] V. Crépel, N. Claussen, N. Regnault, and B. Estienne, Nat. Commun. **10**, 1860 (2019).

[62] V. Crépel, N. Claussen, N. Regnault, and B. Estienne, Nat. Commun. **10**, 1861 (2019).

[63] V. Crépel, B. Estienne, and N. Regnault, Phys. Rev. Lett. **123**, 126804 (2019).

[64] X. Wan, E. H. Rezayi, and K. Yang, Phys. Rev. B **68**, 125307 (2003).

[65] R. de Picciotto, M. Reznikov, M. Heiblum, V. Umansky, G. Bunin, and D. Mahalu, Nature (London) **389**, 162 (1997).

[66] L. Saminadayar, D. C. Glattli, Y. Jin, and B. Etienne, Phys. Rev. Lett. **79**, 2526 (1997).

[67] M. Dolev, M. Heiblum, V. Umansky, A. Stern, and D. Mahalu, Nature (London) **452**, 829 (2008).

[68] I. P. Radu, J. B. Miller, C. M. Marcus, M. A. Kastner, L. N. Pfeiffer, and K. W. West, Science **320**, 899 (2008).

[69] A. Bid, N. Ofek, H. Inoue, M. Heiblum, C. L. Kane, V. Umansky, and D. Mahalu, Nature (London) **466**, 585 (2010).

[70] M. Banerjee, M. Heiblum, V. Umansky, D. E. Feldman, Y. Oreg, and A. Stern, Nature (London) **559**, 205 (2018).

[71] X.-L. Qi, H. Katsura, and A. W. W. Ludwig, Phys. Rev. Lett. **108**, 196402 (2012).

[72] H. Li and F. D. M. Haldane, Phys. Rev. Lett. **101**, 010504 (2008).

[73] A. Hamma, R. Ionicioiu, and P. Zanardi, Phys. Rev. A **71**, 022315 (2005).

[74] A. Kitaev and J. Preskill, Phys. Rev. Lett. **96**, 110404 (2006).

[75] M. Levin and X.-G. Wen, Phys. Rev. Lett. **96**, 110405 (2006).

[76] A. M. Läuchli, E. J. Bergholtz, and M. Haque, New J. Phys. **12**, 075004 (2010).

[77] J. E. Avron, R. Seiler, and P. G. Zograf, Phys. Rev. Lett. **75**, 697 (1995).

[78] F. D. M. Haldane, Phys. Rev. Lett. **107**, 116801 (2011).

[79] N. Read, Phys. Rev. B **79**, 045308 (2009).

[80] N. Read and E. H. Rezayi, Phys. Rev. B **84**, 085316 (2011).

[81] L. Hu, Z. Liu, D. N. Sheng, F. D. M. Haldane, and W. Zhu, Phys. Rev. B **103**, 085103 (2021).

[82] E. Keski-Vakkuri and X.-G. Wen, Int. J. Mod. Phys. B **07**, 4227 (1993).

[83] W. Zhu, D. N. Sheng, and K. Yang, Phys. Rev. Lett. **125**, 146802 (2020).

[84] S. M. Girvin, Phys. Rev. B **29**, 6012 (1984).

[85] A. H. MacDonald, Phys. Rev. Lett. **64**, 220 (1990).

[86] Y. Zhang, T. Grover, and A. Vishwanath, Phys. Rev. B **84**, 075128 (2011).

[87] M. Haque, O. Zozulya, and K. Schoutens, Phys. Rev. Lett. **98**, 060401 (2007).

[88] B. A. Friedman and G. C. Levine, Phys. Rev. B **78**, 035320 (2008).

[89] A. Sterdyniak, B. A. Bernevig, N. Regnault, and F. D. M. Haldane, New J. Phys. **13**, 105001 (2011).

[90] Z. Liu, D. L. Kovrizhin, and E. J. Bergholtz, Phys. Rev. B **88**, 081106(R) (2013).

[91] M. D. Johnson and A. H. MacDonald, Phys. Rev. Lett. **67**, 2060 (1991).

[92] Please note the total central charge of the $\nu = 8/3$ state is $c = 2$, since the full filled LL of the $\nu = 8/3$ state include two integer chiral edge modes. In the main text, we only consider the $\nu = 8/3$ state in the SLL, so we cannot see the integer chiral edge modes. Conclusively, the central charge of the $\nu = 8/3$ state in the SLL is $c = 0$. By the way, the filling factor in Eq. (27) should be $\nu = 2/3$.

[93] D. Yoshioka, J. Phys. Soc. Jpn. **55**, 885 (1986).

[94] P. Hawrylak, A. Wojs, and J. A. Brum, Phys. Rev. B **54**, 11397 (1996).

[95] U. Khanna, M. Goldstein, and Y. Gefen, Phys. Rev. B **103**, L121302 (2021).

[96] H.-H. Lai and K. Yang, Phys. Rev. B **87**, 125130 (2013).

[97] M. Greiter, Phys. Rev. B **83**, 115129 (2011).